





ECLand: The ECMWF Land surface modelling system

 Souhail Boussetta¹,  Gianpaolo Balsamo¹,  Gabriele Arduini¹,  Emanuel Dutra^{2,3},  Joe McNorton¹, Margarita Choulga¹,  Anna Agustí-Panareda¹,  Anton Beljaars¹,  Nils Wedi¹,  Joaquín Muñoz-Sabater¹,  Patricia De Rosnay¹,  Irina Sandu¹,  Ioan Hadade¹,  Glenn Carver¹, Cinzia Mazzetti¹,  Christel Prudhomme¹,  Dai Yamazaki⁴,  Ervin Zsoter¹

¹ European Centre for Medium-Range Weather Forecasts, Shinfield Park, Reading RG2 9AX, UK 1; Souhail.Boussetta@ecmwf.int (S.B.)

² Instituto Português do Mar e da Atmosfera, 1749-077 Lisbon, Portugal emanuel.dutra@ipma.pt (E.D.)

³ Instituto Dom Luiz, IDL, Faculty of Sciences, University of Lisbon, 1749-016 Lisbon, Portugal;

⁴ Institute of Industrial Science, The University of Tokyo, Tokyo, Japan; yamadai@rainbow.iis.u-tokyo.ac.jp (D.Y.)

* Correspondence: souhail.boussetta@ecmwf.int (S.B.); gianpaolo.balsamo@ecmwf.int (G.B.)

Abstract: The land-surface developments of the European Centre for Medium-range Weather Forecasts (ECMWF) are based on the Carbon-Hydrology Tiled Scheme for Surface Exchanges over Land (CHTESSEL) and form an integral part of the Integrated Forecasting System (IFS), supporting a wide range of global weather, climate and environmental applications. In order to structure, coordinate and focus future developments and benefit from international collaboration in new areas, a flexible system named ECLand which would facilitates modular extensions to support numerical weather prediction (NWP) and society-relevant operational services, e.g. Copernicus, is presented. This paper introduces recent examples of novel ECLand developments on (i) vegetation, (ii) snow, (iii) soil, (iv) open water/lake (v) river/inundation, and (vi) urban areas. The developments are evaluated separately with long-range, atmosphere-forced surface offline simulations, and coupled land-atmosphere-ocean experiments. This illustrates the benchmark criteria for assessing both, process fidelity with regards to land surface fluxes and reservoirs of the water-energy-carbon exchange on the one hand, and on the other hand the requirements of ECMWF's NWP, climate and atmospheric composition monitoring services using an Earth system assimilation prediction framework.

Keywords: Land-surface modelling system; hydrology; carbon; surface energy balance; open water; snow

1. Introduction

Land surface models (LSMs) describe the exchanges of the global energy, water, and carbon fluxes with the land surface and improve our monitoring capacity to predict natural resources and their evolution in time. Besides providing boundary and initial conditions to Numerical Weather Prediction (NWP) systems and Earth System Models in general, land surface models also provide the terrestrial component for several research and operational applications depending on the represented processes and their degree of complexity. LSMs are nowadays used in scales ranging from local to global and sub-hourly to centennial scales through multiple applications going from climate change to hydrological and biogeophysical cycles such as floods and droughts or agriculture and CO₂ monitoring [1–4].

The ECMWF land surface schemes [5–7] are an essential component of the Integrated Forecasting System (IFS) but form also a self-standing model that can be integrated with specified meteorological forcing. In recent years, owing also to modularity of testing in offline and coupled applications,

the land-surface modelling activity at ECMWF has been substantially and continuously expanded. An improved soil hydrology [8], a new snow scheme [9] and a multi-year satellite-based vegetation climatology [10] have been included in the operational IFS. These have had a positive impact on both the global hydrological water cycle and near-surface atmospheric variables compared to the original TESSEL (Tiled ECMWF Scheme for Surface Exchanges over Land) scheme used in ECMWF ERA-40 reanalysis [11] and in the ERA-Interim reanalysis [12], compared to HTESSEL used in ERA5 [13] and ERA5Land [14]. In particular the soil hydrology enhanced the quality of seasonal predictions during extreme events associated with soil moisture-precipitation feedback as in the European summer heat-wave in 2003 [15]. The new snow scheme improved the thermal energy exchange at the surface with a substantial reduction of near-surface temperature errors in snow-dominated areas (i.e. northern territories of Eurasia and Canada) [16]. More recently, the introduction of a monthly climatology for vegetation Leaf Area Index (LAI) to replace the fixed maximum LAI has shown a reduction of near-surface temperature errors in the tropical and mid-latitude areas, particularly evident in Boreal spring and summer. At the same time the bare ground evaporation has been enhanced over deserts by adopting a lower stress threshold than for vegetation. This is in agreement with experimental findings (e.g. [17]) and results in a more realistic soil moisture for dry-lands. Beyond the important day-to-day experience of running the land-surface scheme in an operational NWP environment, the participation in international projects such as GLACE2 (Global Land-Atmosphere Coupling Experiment-2) and AMMA (African Monsoon Multidisciplinary Analysis, [18]), in which the ECMWF IFS model was coupled with a realistic set of soil moisture fields, have improved the understanding of the mechanisms and areas of strong coupling between the land surface and the atmosphere.

With a continuous increase in spatial resolution and more broad applications of LSMs, as well as the growing availability of a range of diverse observations, a clear need for a more complex and accurate process representation is emerging. This continuous research effort aims at improving the land surface model parametrization for better surface prediction and ultimately better NWP and atmospheric composition forecasts. The current improvements are targeting different components of the land surface model, namely, the vegetation parametrization, the snow component, the soil hydrology, the open water/lake parametrization and also the representation of urban areas.

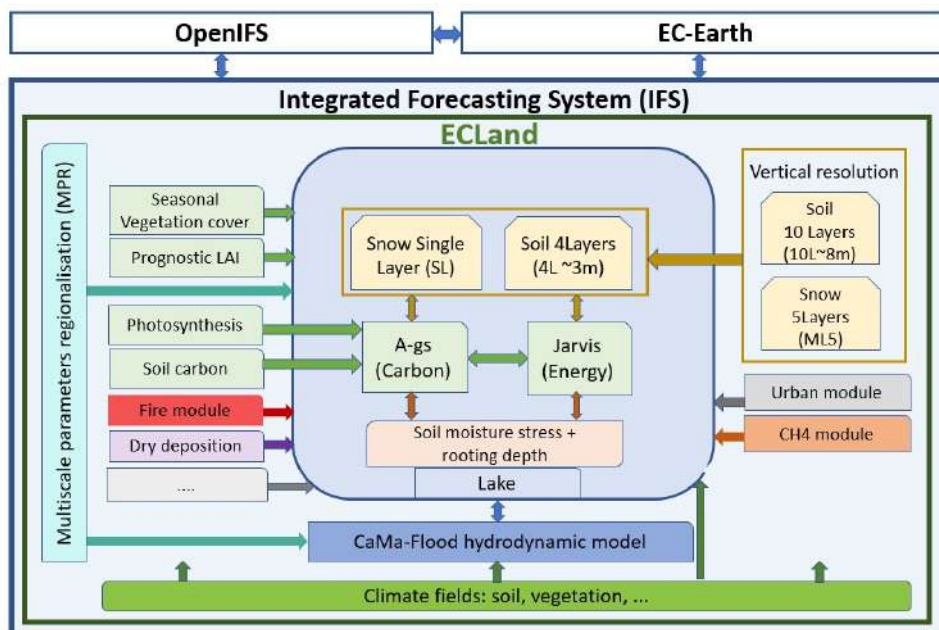


Figure 1. ECLand system components and its prospective evolution and interactions with external projects and services elements as part of the full Integrated Forecasting System.

An efficient and scalable land surface system is essential for a routine NWP and service environment and can facilitate a paradigm shift for an Earth-Observation driven model development (Balsamo *et al.* [19]) under an Earth System framework, while linking with new possibilities brought by machine learning and Artificial Intelligence (AI) tools (Reichstein *et al.* [20]). The ECMWF land surface model has evolved as a modelling system (ECLand) that would facilitate such modular extensions for the benefit of efficient developments and external collaborations. Figure 1 illustrates the ECLand system components and its prospective evolution elements as it would interact with external projects and modular added services, being part of the full Integrated forecasting system. Important criteria for incorporating land-surface developments into ECLand are: *Observability*, e.g. EO-data driven Calibration/Validation and Initialization, and added complexity if there is a route to successfully initialise and verify; *Relevance* for NWP and Copernicus applications, e.g. leading to a substantial product enhancement; *Impact* on coupled Earth System forecast performance and key products, e.g. improving NWP, extended range or seasonal atmospheric forecast skill, or providing skilful products for Copernicus services.

There is a long track record of participation in model intercomparison projects facilitated by WMO (e.g. GEWEX, WGNE), which above all verifies and validates different approaches, and sets standards for model development while identifying and publicising systematic model errors, model uncertainty and shortcomings. It also illustrates needs for added complexity and thus makes the case for any of the above criteria, namely observability, relevance, or impact. Meaningful examples are PLUMBER [21,22] dedicated to benchmarking, or the Earth2Observe FP7 project [23] where ECMWF provided high quality standardly formatted global meteorological forcing and coordinated a first multi-model Water Resources Reanalysis based on ERA-Interim/Land experience [24]. For hydrology, C3S assets such as ERA5L [14] motivated the ULYSSES project within the C3S sectoral hydrological applications with an offline multi-model stream. For Carbon, the CHE Horizon 2020 project [25] within the ECMWF CO₂ activities, have established ECMWF as a European CO₂ monitoring integrator and will within CoCO₂ project coordinate a land multi-model benchmarking activity. This will be supported by experience gained within the Numerical Weather Prediction, for which a set of land-atmosphere coupling development priorities have been defined [26].

This paper describes the ECMWF land surface modelling system ECLand and a snapshot of its new developments. ECLand is based on the previous CHTESSEL parametrization with recent new developments focusing on the improvement of NWP within an earth system modeling concept. The recent developments aim at supporting new research questions in weather, hydrology, climate and environmental applications, ultimately at global kilometric-scale spatial resolution.

The configuration used in ECMWF's operational NWP is described in the next section (model description), followed by ongoing developments aimed at improving the model and its application in the model developments section. An evaluation of the different new components is then performed, depending on the nature of the change with offline and/or coupled simulations, in section 4 (evaluation of model developments) and a final section presents a summary and future perspectives.

2. Model description

This section introduces the current land surface parameterisation operationally used at ECMWF. It describes the representation of the land surface fluxes of energy, water and carbon, and where appropriate, corresponding sub-surface quantities. The main surface scheme parameterisation structures were set with the Tiled ECMWF Scheme for Surface Exchanges over Land [5–7]. At the interface between the surface and the atmosphere, each grid-box is divided into fractions (tiles), with currently seven fractions over land (bare ground, low and high vegetation, intercepted water, shaded and exposed snow and lake) and up to two fractions over sea and freshwater bodies (open and frozen water). Each fraction has its own properties defining separate heat and water fluxes used in an energy balance equation solved for the tile skin temperature (see the supplementary material

for detailed formulation). Special attention is devoted to the different physical mechanisms limiting evaporation of bare ground and vegetated surfaces.

One of the important characteristics of the ECMWF land surface scheme is the short time scale associated with the skin layer, that allows the skin temperature equation to be solved implicitly together with the vertical turbulent transport in the boundary layer, as a natural integrated way within the IFS. In a fully implicit approach, the tiles' skin temperatures depend on each other and can not be solved independently. Therefore the coupling approach suggested by Best *et al.* [27], which allows for such a solution, is used.

A revised land surface hydrology [8] was introduced to address shortcomings of the previous version, specifically the lack of surface runoff and the choice of a global uniform soil texture. New infiltration and runoff schemes were introduced with a dependency on the soil texture and standard deviation of orography. The snowpack is treated taking into account thermal insulation properties, snow density, interception of rain and the evolution of the albedo due to metamorphism aging processes [9,28].

Over land, the skin temperature is in thermal contact with a multi-layer soil (currently 4 layers, cf section 3.3) or with a snow layer mantle overlying the soil, if snow is present (section 3.2.1). The snow temperature varies due to the combined effect of top energy fluxes, basal heat flux and the melt energy. The soil heat budget follows a Fourier diffusion law, modified to take into account the thermal effects of soil water phase changes. The energy equation is solved with a net ground heat flux as the top boundary condition and a zero-flux at the bottom. Further details are described in the supplementary material.

Snowfall is collected in the snow mantle, which is in turn depleted by snowmelt, contributing to surface runoff and infiltration. A fraction of the rainfall is collected both by the snow mantle and by an interception layer, where the remaining fraction (throughfall) is partitioned between surface runoff and infiltration. Subsurface water fluxes are determined by Darcy's law, used in a soil water equation solved with a multi-layer discretization shared with the heat budget equation. The top boundary condition is infiltration plus surface evaporation, free drainage is assumed at the bottom; each layer has an additional sink of water in the form of root extraction over vegetated areas. The seasonal evolution of the vegetation growth modulates the evapotranspiration [29], and a revised formulation of the bare soil evaporation improves the realism of soil-atmosphere water transfer over sparsely vegetated areas and deserts [30].

The land surface exchange of carbon dioxide (CO₂), which represents an essential component of the green-house-gases global budget, has been added [10] to enable the interaction with atmospheric CO₂ concentration in environmental forecasting applications. Land CO₂ responds to meteorological and climate disturbances and is modulated by the natural biomes diversity and their stress conditions. The main photosynthesis processes fixing carbon dioxide into biomass and releasing carbon dioxide via land biogenic processes are parametrized, while land carbon stocks are made dependent on land-use. The carbon parametrization is modular to the land surface scheme water cycle parametrization and it introduces the capability of interacting with the atmospheric CO₂ concentrations for global monitoring and prediction purposes.

Finally, open water tiles classified as lakes and any subgrid water area are treated by a dedicated mixed layer model (31, 32, 33). Open ocean points have a specified surface temperature driven by initial and boundary conditions that in ocean coupled simulations are driven by the ocean model tendency. Sea-ice occupies a fraction of the grid box specified by a sea-ice cover, while lakes and coastal ice are treated by dedicated prognostic variables in the lake model. The sea ice prognostic temperatures are evolving in the forecast following the heat budget of a four-layer ice model in thermal contact with underlying ocean at freezing temperature. The lakes and coastal ice temperatures evolve following a single layer ice scheme with an underlying water at freezing temperature.

The CO₂-enabled land surface scheme, which includes the lake and subgrid water treatment, is the version currently used in the operational IFS system (CY47R1) and is also the base of the ERA5Land

land reanalysis [14]. For the sake of completeness, a detailed mathematical description of its different components is provided in the supplementary materials and the related cited papers. In this paper, the model configuration based on operational IFS cycle (CY47R1) supporting daily forecasting from June 2020 will be referred to as the "current" model version.

ECLand encompasses the current model version, operational in 2021 and results from research developments that are foreseen entering in upcoming model upgrades and detailed in the next section.

3. Model development

A continuous effort is made to improve the realism of surface-atmosphere interactions and to keep the model up-to-date with regard to state-of-the-art developments. The efforts described below are motivated by (i) the need to reduce biases and deal with compensating errors within the coupled NWP framework [26], (ii) the need to improve process-based parametrizations given the continuous increase in spatial resolution and the broader application spectrum, and (iii) the need to use more accurate and up-to-date ancillary data to deal with very high spatial resolution and reduce representativity errors. Hereafter we introduce ongoing research work with different levels of maturity which are available in ECLand as configurations that can be activated independently or jointly. These developments are also categorised as ready for operational implementation or operationally viable for upcoming cycles.

3.1. Land biosphere representation

The vegetation developments that compose the land biosphere model are twofold, one focuses on the upgrade of the vegetation related maps, the other focuses on the improvement of the vegetation dynamics in time.

3.1.1. Land use/Land cover and Leaf Area Index

Current Land Use/Land Cover (LU/LC) are from the dated GLCCv1.2 data ([34] which is based on observations from the Advanced Very High Resolution Radiometer (AVHRR) covering 1992-1993. An upgrade to more accurate and up-to-date vegetation LU/LC maps is introduced with a new automated framework that enables an easy use of the latest maps. These new maps are based on the ESA-CCI LU/LC brokered through the Copernicus Climate Change Services (C3S) which provides consistent maps at 300 m spatial resolution on an annual basis from 1992 to present (currently 2019). The maps have a total of 22 land cover classes based on the land cover classification system (LCCS) developed by the United Nations Food and Agriculture Organization (UN FAO). To be used in the model, the 22 LCCS classes are converted to the Biosphere-Atmosphere Transfer Scheme (BATS) classes through a new cross-walking table which allows removing "residual" (non pure) vegetation types such as the interrupted forest (which covers about 25% of the land points in the current ECMWF maps. It is important to note that having actual/pure plant types allows a better characterization of the model parameters, especially for parameters based on observed quantities.

The difference in high and low vegetation covers between ESA-CCI and GLCCv1.2 based maps (Figure 2) shows an increase of low vegetation cover at the expense of the high vegetation cover in forest areas and a decrease of low vegetation cover favouring more bareground, especially over the Siberian and Australian deserts. The vegetation types show a split of the mixed and interrupted forest types between pure forest and low vegetation types. These differences suggest a substantial impact on the energy fluxes which will be explored in the evaluation section.

Additional developments are focused on improving the model phenology and its seasonality which is represented in the model by the Leaf Area Index (LAI). To be used in the model with the tiles concept, the LAI needs to be split into low and high vegetation components. An update of this LAI disaggregation operator is developed. The current operator tends to overestimate the LAI during the transition periods (spring and autumn), while the new operator is more conservative of the observed LAI. The currently used operator relies on a LAI lookup table that represents the yearly maximum LAI per vegetation type and applies a seasonal cycle based on a MODIS LAI climatology [10]. The new

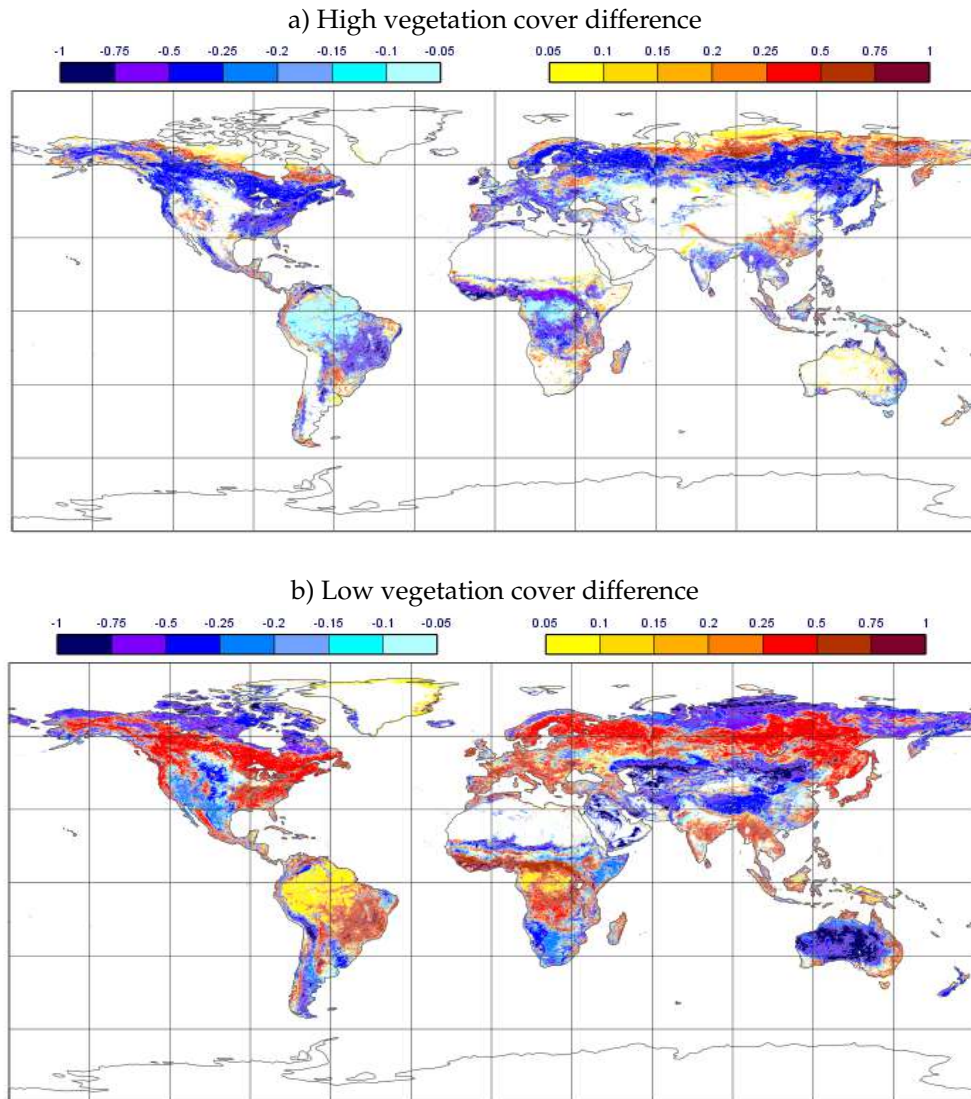


Figure 2. Vegetation cover difference: ESA-CCI - GLCCv1.2 based maps

operator extracts a seasonally varying LAI lookup table per vegetation type. In combination with the vegetation types map it defines the ratio of low and high LAI components which is then applied to disaggregate the satellite based climatological LAI. The revised operator allows thus to derive low and high LAI climatology components which when combined tend to conserve the observed total LAI climatology, in particular for the transition seasons. It also prepares for an operational assimilation of the LAI to allow better monitoring of the surface conditions inter-annual variability and representation of extremes as found in Boussetta *et al.* [35]. Following the changes in the high and low vegetation coverages, figure 3 shows that for July the new LAI components tend to increase for high vegetation by up to 80%, while for low vegetation it mostly decreases by up to 60% in low vegetation dominated areas. In January (not shown) both low and high vegetation LAI tend to decrease by up to 80% compared to the current values.

3.1.2. Dynamic vegetation

Taking into account vegetation dynamics in ECLand involves two different steps: in the first, dynamical vegetation cover is considered, and for the second, a prognostic phenology is developed.

Seasonal vegetation cover

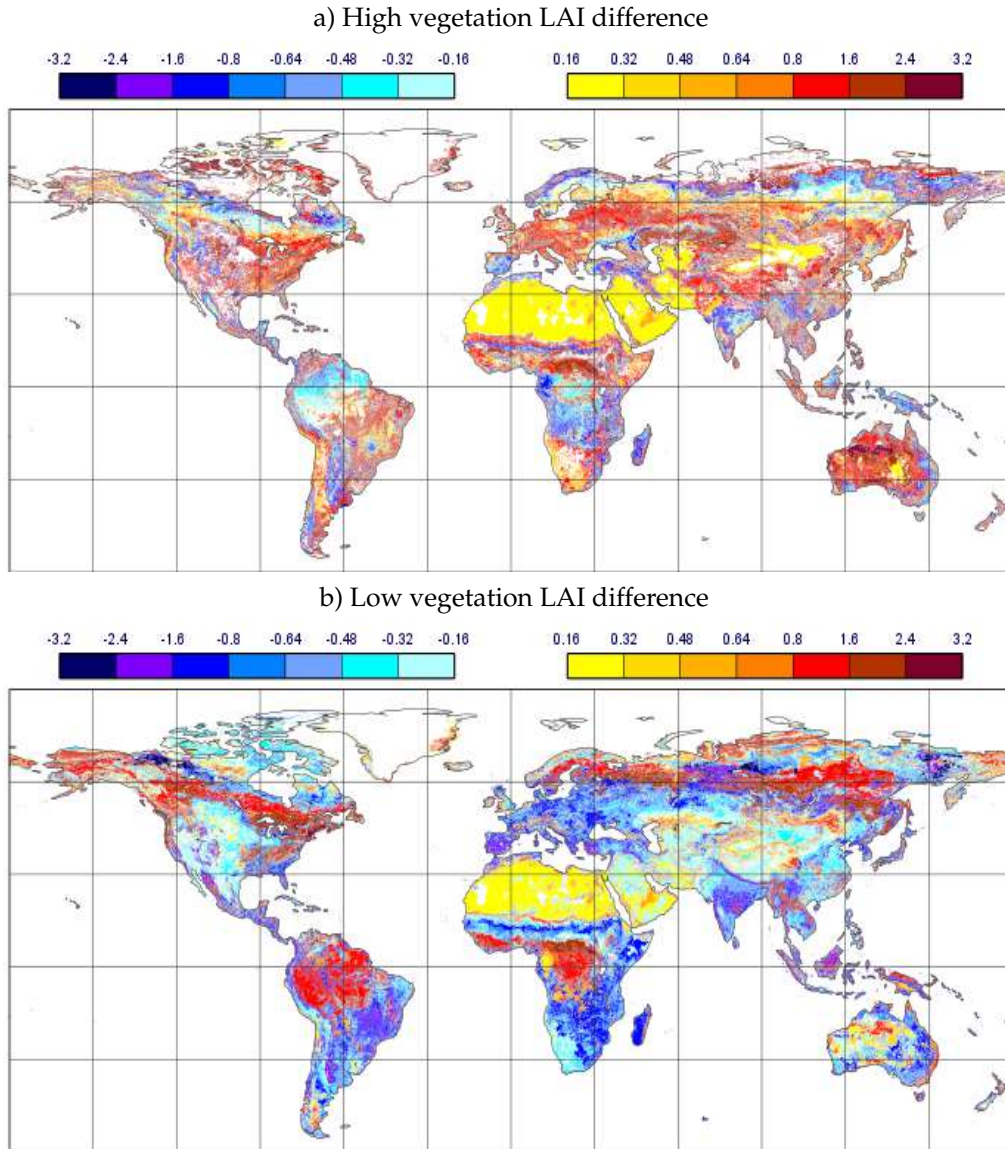


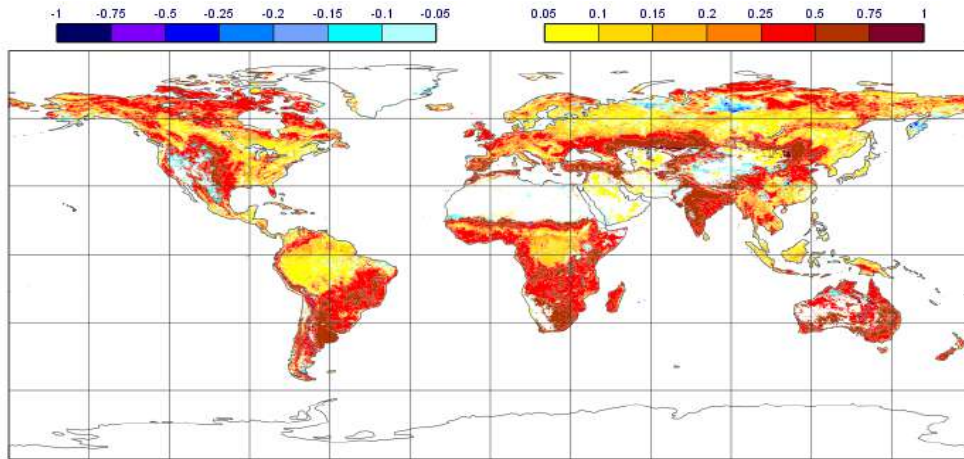
Figure 3. LAI differences for the month of July: Conservative disaggregation - Current

Unlike albedo and LAI, for which seasonality is taken into account, the current vegetation cover is implemented as a fixed map with no seasonal or inter annual variability. In the new development, the seasonality of the vegetation cover is introduced by linking it to the LAI seasonality through the Lambert-Beer formulation and considering the vegetation clumping ([36]). The vegetation density C_{veg} is expressed as:

$$C_{veg} = 1 - e^{-k \cdot LAI} \quad (1)$$

where k is a coefficient dependant on the vegetation clumping for low or high vegetation. Typical values of k range between 0.4 and 0.8, here we consider a value of 0.6 which was also adopted by Nogueira *et al.* [37]. In the latter study, when the clumping was also applied to the high vegetation, coupled simulations indicated a strong impact over the Northern Hemisphere circulation which require further investigations, therefore the implementation in this study is so far limited to low vegetation.

a) Bareground fraction difference between seasonal varying and static vegetation (July).



b) Low vegetation cover difference between July and January

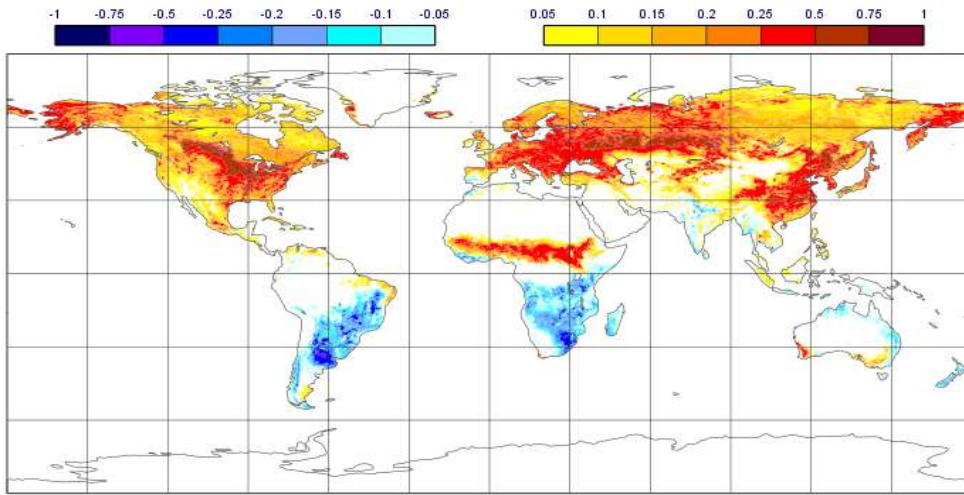


Figure 4. The effect of seasonal varying vegetation cover. a) Bareground fraction difference between the seasonally varying and the static vegetation map for July. b) The seasonal amplitude of low vegetation cover as difference between July and January

Prognostic vegetation phenology

The Leaf Area Index is simulated with a simple growth model based on the daily carbon balance at the leaves level following Gibein *et al.* [38] and Calvet and Soussana [39]. The LAI is computed from the leaf biomass B derived from the net canopy assimilation A_{nI} . Growth is the result of carbon accumulation obtained from assimilation of atmospheric CO_2 and senescence related to the photosynthesis deficit due to environmental factors. LAI is obtained from the product of the green leaf biomass B with the Specific Leaf Area (SLA) which is a function of leaf nitrogen concentration dependent on vegetation types following:

$$LAI = B \cdot SLA = B \cdot e \cdot N_l + f, \quad (2)$$

where N_l is the leaf Nitrogen concentration, and e, f are respectively the slope and intercept nitrogen plasticity parameters which vary by vegetation types. For global scale applications and to reduce drifts caused by forcing errors, the computed biomass is updated by a relaxation formulation toward climatological biomass values B_C (based on climatological LAI), the final biomass value B_f follows:

$$B_f = r_B \cdot B + (1 - r_B) \cdot B_C, \quad (3)$$

where r_B is the relaxation coefficient. For the sake of completeness, the growth model is further detailed in the supplementary materials.

3.2. Updated snow parametrization

3.2.1. Structure of the multi-layer snow scheme

The multi-layer snow scheme (ML hereafter) introduced in ECLand is an intermediate complexity snow scheme following the definition by Boone and Etchevers [40]. It represents the vertical structure and evolution of snow temperature, density, liquid water content and snow albedo. A comparison of the structures of the single layer (SL) and ML and the coupling to the atmosphere and soil is shown in Fig. 5. ML uses the same parametrizations of snow cover fraction and albedo (both for exposed and forest snow) as in SL. A preliminary version of ML implemented in the EC-EARTH climate model was reported by Dutra *et al.* [16] and tested in long climate simulations. In the following, only the main characteristics of ML are described and a detailed description of the scheme is reported in Arduini *et al.* [41].

The heat budget of the snowpack is solved implicitly for the active snow layers, and using an explicit flux coupling at the snow-atmosphere interface [42]. To ensure numerical stability over forested areas, the skin heat conductance (inverse of skin resistance $r_{sk,7}$, see Fig. 5) in the surface energy balance calculation is modified following Beljaars *et al.* [42]. The bottom boundary condition is formed by the residual of the heat fluxes at the bottom of the snowpack and the conductive heat flux (G_B) between the snow and soil interface.

Melting and freezing processes are diagnosed in ML by computing the heat content of each snow layer sequentially from top to bottom, after that the heat budget is solved in absence of melting (first-guess of the snow temperature). Movement of liquid water between layers (meltwater or rainfall) is taken into account using a bucket-type formulation as in [16]. The latent heat released or absorbed during phase changes in a snow layer is used to vary the temperature of the respective snow layer.

The number of active snow layers and their thicknesses is computed diagnostically at the beginning of each time-step before the prognostic snow fields are updated. The number of active layers (N) varies depending on snow depth D_{sn} , from a minimum number of 1 layer to a maximum of $N_{max} = 5$. Multiple layers are used when the grid box is completely snow-covered, that is for $D_{sn} \geq 0.1$ m. As opposed to Arduini *et al.* [41], a different discretization algorithm is applied over flat terrain and complex terrain regions, the latter defined as regions with the standard deviation of the sub-grid-scale orography greater than 50 m. Over flat terrain, for $D_{sn} > 0.1$ m the thickness of the topmost layer in contact with the atmosphere is fixed to 0.05 m. The thickness of the other active snow layers can increase up to a certain maximum D_i^{max} , as described in Arduini *et al.* [41]. For a thick snowpack, the layer $N_{max} - 1$ is used as an accumulation layer, enabling a relatively high vertical resolution at the interfaces to be maintained with the atmosphere above and the soil underneath. An example of the vertical discretization of a 1.0 m-thick snowpack is shown in Fig. 5c.

Over complex terrains, for $D_{sn} < 0.25$ m the same vertical discretization as described for a flat terrain is used. For a snowpack with $D_{sn} \geq 0.25$ m, the minimum ($D_{min,i}$) and maximum ($D_{max,i}$) thicknesses of each layer (i.e. the minimum and maximum allowed thickness for an active snow layer) varies with snow depth as follows:

$$D_{min,i} = \min(0.25, 0.10 + \alpha_o (D_{sn} - 0.25)) \quad \text{if } i = 1 \dots N_{max}$$

$$D_{max,i} = \begin{cases} \min(0.25, 0.10 + \alpha_o (D_{sn} - 0.25)) & \text{if } i = 1 \\ \min(0.30, 0.15 + \alpha_o (D_{sn} - 0.25)) & \text{if } i = 2 \dots N_{max} \end{cases}$$

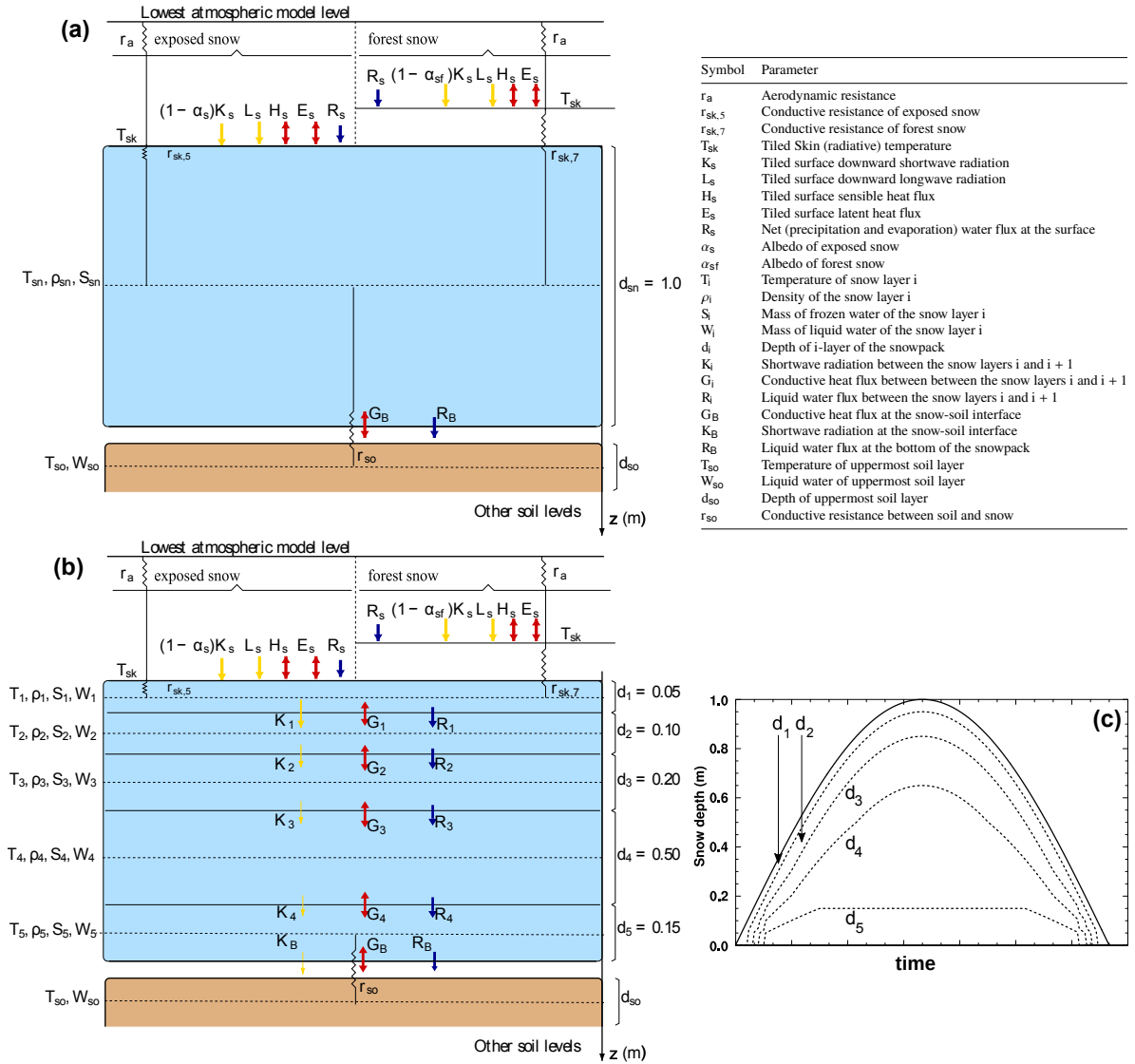


Figure 5. Schematics of the (a) single-layer and (b) multi-layer snow schemes, for a 1-metre thick snowpack. In (b), the vertical discretization of such a snowpack (d_1, \dots, d_5 , in m) for flat terrains is also shown. (c) Idealized time-series of snow depth accumulation and ablation (continuous line) with the vertical discretization used in the multi-layer scheme. The list of symbols used in (a) and (b) is also reported

with α_0 set to 0.10. This implies that for a thick snowpack over complex terrain the snow layers are thicker than a snowpack with same depth over a flat region. A full description of the vertical discretization algorithm is detailed in Arduini *et al.* [41].

3.2.2. Changes in the snow physics parametrizations

In addition to the structural aspects described above, ML differs from SL also in the parametrization of the following physical processes:

- (I) The heat conductivity is parametrized using the formulation of Calonne *et al.* [43] and taking into account the water vapor diffusion effects following Sun *et al.* [44];
- (II) Transmission of solar radiation decreases exponentially with depth and it is parametrized using a formulation adapted from Jordan [45];
- (III) Density variations due to wind transport (snowdrift) are taken into account, in addition to the other compaction processes. This can be particularly effective for polar snow, for which snow

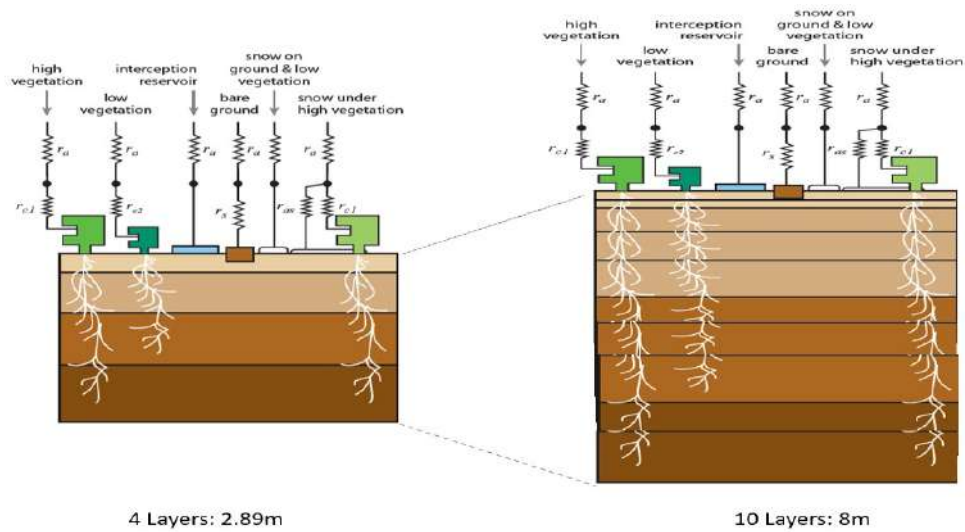


Figure 6. Updated soil depth and vertical discretization

- temperature is extremely low throughout the winter, and compaction due to other processes is limited [46,47]. Wind-driven compaction is parametrized using a mobility index combined with a wind-driven compaction index, following Decharme *et al.* [47];
- (IV) The basal heat conductivity (r_{so}) is computed using a new physical formulation using the snow and soil thermal conductivities as described in Arduini *et al.* [41].

3.3. Updated soil parametrization

With higher spatial resolution and more accurate grid parameters characterisation, in addition to broader applications and the need to improve the water budget in the model and coupled hydrological components, the importance of the soil depth and vertical discretisation within land surface models has increased. It affects the way land surfaces store and regulate water, energy and also carbon fluxes. The amount of water in the soil and its vertical distribution in the column are important for the regulation of heat and water vapour fluxes towards the atmosphere spanning a range of time scales from minutes to months in the coupled land-atmosphere system. This is further modulated by the vertical roots distribution, and soil moisture stress function, which control evapotranspiration under soil moisture stress conditions (next section). Currently in the ECMWF land Surface Scheme the soil column is represented by a fixed 4-layer configuration with a total of 2.89m depth. In the ECLand system we introduce new configurations with increased soil depth (up to 8m) and higher vertical discretisation (up to 10-layers), including a dissociation between the treatment of water and heat fluxes (Figure 6) following [48]. In these configurations, the upper layers also have thinner depth allowing a better match with satellite soil moisture observations.

An optional formulation for the distribution of roots density has been also developed in ECLand. It is based on a uniform distribution, which is appealing due to its simplicity and straightforward first-order assumption. This uniform distribution replaces the current exponential formulation and depends only on the maximum rooting depth (R_{DMAX}). This root distribution formulation was investigated by Stevens *et al.* [49] and showed potential for improvement of the water and energy fluxes. The transformation of root zone soil moisture to water stress is also an open question, and there are different approaches to relate root zone soil moisture and the water stress factor [50,51]. In ECLand it is also possible to change the linear transformation between root zone soil moisture and water stress by a non-linear relation, which showed a large sensitivity in offline and coupled forecasts [52]. Such approaches, combined with the rooting depth distribution, are likely to further enhance the model capability to represent root water uptake, but require further evaluation and calibration.

3.4. Surface water representation

An upgraded versions of the physiographic datasets used in ECLand to generate the land sea mask and the lake parameters is described. In addition to the ecosystem data, the new land-water mask uses a newly generated glacier data and a new land-water and lake fraction mask. The lakes are also benefiting from updated lake depth data. The main data sources for land-water mask are from the Joint Research Centre (JRC) with nominal resolution 30 m (1"). The high resolution information at 30m is used in the data merge then aggregated to 1 km.

The upgraded inland water mask is based on the upgraded fractional land-water mask at 1 km resolution. First, fractional land-water mask is translated into "land" and "water" binary mask, then by using an innovative "waterbody" separation algorithm [53] "water" is separated into ocean and inland water bodies. The algorithm is pixel-by-pixel and iterative based on the spatial window width, and the number of iterations which depends on the resolution and complexity of the coastline. At the end of all iterations a visual check is needed to correct freshwater coastal lagoons where needed. The Azov sea and Maracaibo lake are also processed as inland water given that they are better represented in the model by the lake parametrization which illustrates some of the assumptions required in this process. Figure 7 illustrates the main differences from the new land water mask and the current operational one (CY47R1). It shows that several inland water (lake) appear in the new map especially in north Canada and Russia while some lakes are removed from central Australia. Detailed description of the data sources and the processing chain for the updated surface water is provided in the supplementary material.

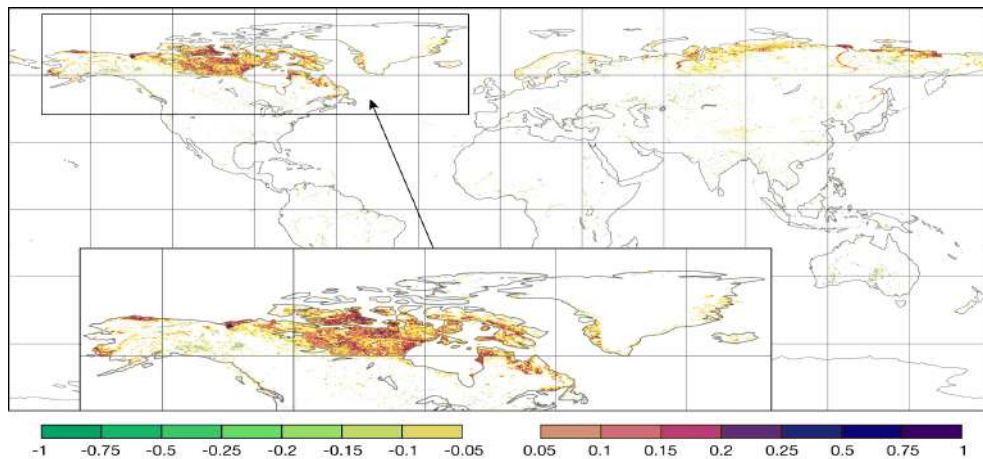


Figure 7. Lake cover difference: new GSWE based - operational map

3.5. Coupling with a hydrodynamic model

River discharge is a key component of the global water cycle, integrating meteorological and hydrological conditions on multiple temporal and spatial scales. The increased skill of numerical weather prediction has led to the uptake of weather forecasts products by hydrological models, for example in flood forecasting [54]. At the same time, the developments of Earth System Models, mainly driven by the climate community, resulted in a tight integration of atmospheric models and the surface water balance [55]. River discharge is a key quality indicator of the integrated water budget, and therefore its use as a forecast skill metric has significant potential [56]. Furthermore, freshwater input to the ocean is also important for the ocean circulation, which becomes increasingly relevant with the current atmosphere-ocean coupling in numerical weather prediction as in Zuo *et al.* [57]. Considering all these points, the representation of rivers and their associated role on the land and ocean water is of interest for a wide range of applications. This motivated the integration of the Catchment-based Macro-scale Floodplain model (CaMa-Flood) into the ECLand system.

CaMa-Flood is designed to simulate the hydrodynamics in continental-scale rivers. The entire river networks of the world (excluding Antarctica) are discretized to hydrological units named unit-catchments for achieving efficient flow computation at the global scale. The water level and flooded area are diagnosed from the water storage at each unit-catchment using the sub-grid topographic parameters of the river channel and floodplains. By adapting a “grid-vector hybrid river network map” which connects one irregular-shaped unit-catchment to one rectangular grid-box, both a realistic parametrization of sub-grid topography and an easy data handling are achieved. The river discharge and flow velocity are calculated with the local inertial equation [58] along the river network map which prescribes the upstream-downstream relationship of unit-catchments. There is also an option to compute flow velocity using a kinematic wave approximation. The time evolution of the water storage, the only prognostic variable, is solved by the water balance equation which considers inflow from the upstream cells, outflow to the downstream cell and input from runoff forcing at each unit-catchment. The detailed description of the CaMa-Flood model is found in the description papers [59–61].

The key characteristic of CaMa-Flood is the explicit representation of flood stage, representing water level and inundation extent, which complements the conventional use of river discharge [62]. This also allows exploring two-way coupling with the land surface model [63]. The baseline topography is based on MERIT DEM/MERIT Hydro [64,65]. River channel width is objectively parametrized using satellite measurement [66,67].

CaMa-Flood source code is integrated in the ECLand system allowing stand-alone CaMa-Flood simulations or simulations with 1-way and 2-way coupling between ECLand and CaMa-Flood. The coupling is performed sequentially and the code is integrated as a single executable (without external couplers) following a similar approach as the coupling with the ocean model to IFS [68]. In 1-way coupling, the default configuration, surface and sub-surface runoff are sent to CaMa-Flood. In stand-alone mode CaMa-Flood reads from input files the runoff data, reproducing the 1-way coupling results. This configuration has a lower computational cost, allowing for testing of the hydrodynamic model as well as driving the model with other runoff data sources like reanalysis. The 2-way coupling between ECLand and CaMa-Flood was also experimentally developed allowing initial testing of the interaction between inland water in ECLand and flooded areas in CaMa-Flood. Inland water evaporation (in ECLand) can be extracted from flooded areas in CaMa-Flood, and the flooded area extent can update the inland water fraction in ECLand. CaMa-Flood integration in the ECLand system is only available in offline mode supporting shared memory parallelism via OpenMP. A full integration of CaMa-Flood in the IFS is envisaged in upcoming cycles to support coupled atmosphere-ocean-land-rivers simulations aiming at a full representation of the water cycle. This will still require developments both at the level of distributed memory parallelism in CaMa-Flood and in the coupling of river discharge with the ocean model.

The river network description used in CaMa-Flood is currently available in several global regular latitude/longitude resolutions: $1/4^\circ$, $1/10^\circ$, $1/12^\circ$, $1/20^\circ$, and $1/60^\circ$. However, each unit-catchment in CaMa-Flood has an irregular shape and ECLand can be setup on any regular or the IFS model’s Gaussian reduced grid. To accommodate the different spatial grids between these two components, the fluxes are interpolated using pre-computed weights that account for the area of interception of each grid element. For the 2-way coupling, the inverse of the weights is used to guarantee mass conservation. These weights are computed as part of the pre-processing of the system, which also allows the definition of regional domains, which are relevant for testing and for applications that do not require the global setup.

3.6. Urban parametrization

A single-layer-type urban model (Figure 8) is implemented within ECLand. The Urban scheme is applied as a new sub-grid surface tile and uses mapped parameters and derived variables to compute surface energy and hydrology fluxes. The urban environment is represented as both a canyon,

consisting of walls and road, and a roof fraction. An infinite length canyon assumption is made to factor shadowing from buildings and is dependent on both urban parameters and the solar zenith angle. Building height and canyon characteristics are used to estimate surface roughness and any concept of canyon orientation is removed. Energy and moisture exchange between the surface and both the atmosphere and sub-surface is defined by urban parameters, including a simple representation of urban drainage. The scheme consists of both time varying (e.g. albedo based on solar zenith angle) and fixed variables (e.g thermal heat capacity of a building). The variables required for the urban scheme are based on previous similar schemes ([69], [70], [71]) and listed in the supplementary material.

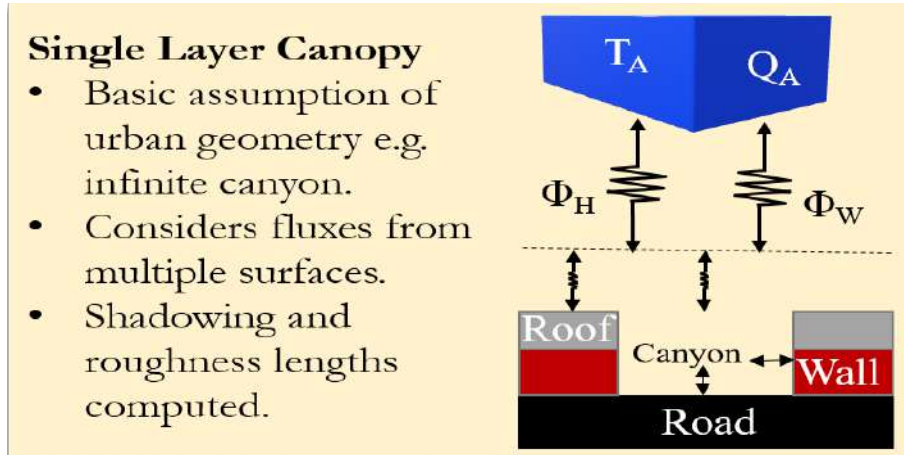


Figure 8. Schematic of the single-layer urban model type used in NWP models, including representation of heat and moisture content of the atmosphere and surface as well as fluxes. (Adapted from [72])

Currently ECLand, consists of 8 sub-grid surface tiles and a lake tile. To represent the urban environment we have introduced a tenth tile and updated the high vegetation snow to include an urban representation. When considering tile fractions over land, the value summed across all tiles is equal to 1. For the land surface this was previously a combination of wet land, low vegetation, high vegetation and bare soil and, for the latter 3 with and without snow cover. Over urban areas the addition of an urban land cover map would increase the sum above 1. To prevent this, existing tile fractions are re-weighted to account for the urban tile following an update of the ECLand tiles equation 4 where high vegetation (C_H), low vegetation (C_L), bare soil (C_B) and snow under high-vegetation ($C_{H_{snow}}$) covered fractions are updated from the original values ($C_{H_{orig}}$, $C_{L_{orig}}$) accounting for the urban fraction (C_U).

$$\begin{aligned}
 C_H &= C_{H_{orig}} \times (1 - C_U), \\
 C_L &= C_{L_{orig}} \times (1 - C_U), \\
 C_B &= (1 - C_H - C_L - C_U), \\
 C_{H_{snow}} &= C_{sn} \times (C_H + C_U), \\
 C_{U_{dry}} &= (1 - C_{wet}) \times (1 - C_{sn}) \times C_U,
 \end{aligned} \tag{4}$$

where C_{sn} , $C_{U_{dry}}$ and C_{wet} represent the snow covered, dry urban and wet fraction, respectively.

For land surface skin, future developments will merge the urban cover product with the remaining land cover so this re-weighting process is no longer required. For certain elements, e.g. hydrology, this prevents a weighted average that neither fits an urban or non-urban regime. Currently, for sub-surface thermodynamic and hydrological properties, the urban tile re-weights the uppermost soil layer. The urban land cover used here is based on grid cell specific information provided by ECOCLIMAP-SG, at an initial 300 m horizontal resolution [73].

3.7. Model efficiency

The surface model inherits the same "array-block" data structures as all other IFS physics parameterisation packages and is therefore capable of benefiting from modern processors and GPUs. These data structures allow for the exploitation of shared memory parallelism via OpenMP as multiple threads can work independently on distinct array-blocks, therefore leading to a reduction in memory consumption and improved load balancing, with the scaling of these blocks tailored depending on the target architecture. This makes ECLand a very well adapted and efficiently integrated component of the IFS. The offline ECLand model version equally supports distributed memory parallelism via the Message Passing Interface (MPI). The new implementation allows to significantly accelerate the computational performance of ECLand in offline mode at all resolutions and enables efficient simulation at very high resolutions such as 1km (with a throughput of one year of global simulation per day). This throughput is important for a range of new developments including accounting for urban areas (see section 3.6, Figure 26) and their carbon emissions within the future Copernicus CO₂ service as well as the foreseen developments under the Destination Earth initiative (DestinE), which aims at creating a high-precision digital twins of the Earth [74].

One of the largest scalability bottlenecks when running ECLand in offline mode at very high resolutions (e.g., 1km) is input/output (I/O). Ongoing development would attempt to mitigate this by exploiting the capabilities of modern parallel file systems and higher level libraries such as NetCDF4. Parallel efforts focus to consistently adapt ECLand to ECMWF's multi-IO development including optional output in different formats such as NETCDF or GRIB2.

Additional development towards increased model efficiency is the ability to run on accelerated hardware such as Graphics Processing Units (GPUs). An effort towards porting the surface model to run efficiently on GPUs has already started at ECMWF under the umbrella of the Scalability programme [75].

4. Evaluation of model developments

4.1. Data and methods

New developments are usually evaluated with either offline or both offline and coupled forecasts depending on their target applicability and level of testing. For specific applications, only offline land surface modeling is needed while for others, coupled simulations are necessary, e.g if the land-atmosphere interactions affect the simulation results. For implementation within the ECMWF operational IFS, a more strict assessment is adopted: new developments are evaluated offline, in coupled forecasts and data assimilation configurations. More recently, under the concept of earth system modelling, hydrology related scores, which introduce additional constraints for uncertain parameters, started to be also considered aiming at improving the core objective of NWP as well as other earth system applications. To characterize the impact of the new developments mentioned in this paper, the model performance is evaluated independently according to each developments' level of maturity following the configurations described in table 1. In this paper, hydrological verification is only performed for the coupling with the river discharge development. All 2D and 3D simulations are run at the Tco399 Gaussian octahedral grid (25km), the offline simulations are driven by the ERA5 atmospheric forcing while the coupled forecast simulations are initialized with corresponding offline simulations to avoid unstable surface conditions related to spinup problems.

Table 1. Experimental configurations for the evaluation of model developments

Model development	Experiment type	Name	Comment
Surface water representation	Offline Surface simulation	OSW	Updated lake parameters
	Coupled Forecast + Data assimilation	DASW	Updated Glacier, Land water mask and lake
Updated LU/LC and LAI	Offline Surface simulation	CLAI	ESA-CCI land cover and LAI conservative disaggregation
	Coupled simulation Forecast	FCLAI	
Seasonal vegetation cover	Offline Surface simulation	OSCV	LAI based Seasonal vegetation cover
	Coupled simulation Forecast	FSCV	
Prognostic LAI	Offline Surface simulation	OPLAI	Prognostic LAI based on daily CO2 balance
New snow multilayers	Offline Surface simulation	OSnML5	5 Layers snow scheme
	Coupled Forecast	FSnML5	5 layers scheme
Increased soil depth and discretization	Offline Surface simulation	OSML10_TW	10 Layers soil 8m for temperature and water
		OSML10_T	10 Layers soil 8m for temperature and 3m for water
Coupling with hydrodynamic	Offline Surface simulation coupled with routing model	-	details in section 4.7
Urban parametrization	Offline Surface simulation	OSMU	offline 1D and 2D urban parametrization
	Single Column simulation	SCMU	coupled 1D forecast with urban parametrization

4.2. Observational data to evaluate model developments

The new developments described above are evaluated against the following observations or observation-based products.

FluxCom

The FluxCom dataset (www.fluxcom.org/) is used to evaluate the impact of the new developments on the energy and carbon fluxes. This dataset uses machine learning techniques, namely Random forests (RF), Artificial Neural Networks (ANN) and Multivariate Adaptive Regression Splines (MARS), to upscale FLUXNET in-situ flux observations in space and time and integrate them with remote-sensing and meteorological forcing data. It uses the Moderate Resolution Imaging Spectroradiometer (MODIS) satellite data for the FluxCom-RS version and additionally uses reanalysis meteorological forcing in the FluxCom-RS+METEO version. FluxCom provides fluxes for the RS+METEO version at 0.5° spatial resolution and daily temporal resolution for the 1979-2013 period and the RS version is available at 8-day temporal resolution with 0.0833° spatial resolution for the 2001-2015 period. Further details of the FluxCom data is available in Jung *et al.* [76].

GLEAM

The Global Land Evaporation Amsterdam Model version 3 (GLEAM v3b; Miralles *et al.* [77], Martens *et al.* [78]) is used to evaluate the impact of the vegetation updates on evapotranspiration. GLEAM is a semi-empirical-process-based model that computes evapotranspiration and its components globally over land at daily scale using a set of algorithms driven by satellite-based observations. Potential evaporation is derived over four land cover tiles (low vegetation, tall vegetation, bare soil and open water) using the Priestley-Taylor formulation. Then actual transpiration is calculated by multiplying the potential evaporation by a stress function based on root-zone soil moisture and

vegetation optical depth. Soil moisture is the result of a soil-water balance model that computes the evaporative flux and is driven by observation-based precipitation. The last component of GLEAM is the interception loss which follows the Gash analytical model driven by precipitation and vegetation properties. Further details of GLEAM are documented in Martens *et al.* [78] and Miralles *et al.* [77].

FLUXNET

The FLUXNET data (Baldocchi *et al.* [79]) used are LaThuile in-situ observations (<http://www.fluxdata.org>), a dataset including 253 research sites belonging to the FLUXNET eddy covariance network. This dataset provides latent heat flux (LE), sensible heat flux (H) and net ecosystem exchange (NEE) at high temporal resolution (30 to 60 min) and values for GPP and Reco derived from half-hourly observed NEE following the partitioning method proposed in Reichstein *et al.* [80]. We only used observations flagged as high-quality data, without gap filling.

WOFOST

WOFOST is a crop growth model to estimate yields quantitatively. It is developed by the Department of Theoretical Production Ecology (Wageningen Agricultural University, The Netherlands) and the Center for Agrobiological Research and Soil Fertility (Wageningen, The Netherlands). This model is implemented currently within the MARS Crop Growth Monitoring System (CGMS), allowing the estimation of biophysical variables related with crop yields such as potential biomass production, crop development stage, etc. WOFOST raw simulations are done at soil unit level i.e. for each of the soil types within a soil polygon. These data were provided by JRC under the EU FP7 ImagineS project framework.

LSA SAF LST

Land Surface Temperature (LST) is taken from the Satellite Application Facility on Land Surface Analysis (LSA-SAF). LST is derived from measurements by the Spinning Enhanced Visible and InfraRed Imager (SEVIRI) on board the Meteosat Second Generation (MSG). The LST retrievals are based on the generalized split-window technique [81] and are available every 15 minutes for all clear-sky pixels within the MSG disk with a resolution of 3 km at the nadir. Following previous work on model evaluation with satellite retrievals [37,82], the data is aggregated to a coarser grid (0.25°x0.25°) only keeping the valid pixels (fraction of clear sky). For the comparison with model simulations, clear sky conditions, synchronous in time are considered: (i) at least 70% of the fraction of valid pixels and (ii) total cloud cover lower than 30% [82]. For each day and pixel, when at least 75% of the 3-hourly data was available (6 out of 8), the daily maximum and minimum LST are extracted to compute the diurnal range.

ESA-CCI Soil Moisture

The ESA-CCI soil moisture product (<https://www.esa-soilmoisture-cci.org/>) is also used to evaluate the impact of the new developments on soil moisture. The ESA CCI soil moisture product is provided by the European Space Agency for the 1981-2019 period at 0.25° spatial resolution and daily temporal resolution. It is generated with soil moisture observations from active (ERS1-2 SCAT and MetOp ASCAT A-B) and passive (SMR, SSM/I, TMI, AMSR-E, WindSat, AMSR2 and SMOS) microwave satellite sensors. The combined product is obtained through the assimilation process of both C-band scatterometers active observations that use the change detection algorithm and the passive microwave observed land surface brightness temperature. Further details on ESA-CCI SM data and its generation procedure are found in Gruber *et al.* [83], Dorigo *et al.* [84] and Gruber *et al.* [85].

ESM-SnowMIP

Observations of snow depth, mass and density collected in the Earth System Modelling Snow Intercomparison Project ([ESM-SnowMIP 86]) are important for the evaluation of performance of the new snow scheme at selected sites. ESM-SnowMIP consists of 10 sites at which detailed snow-related observations are available for more than 7 years (some sites more than 15 years) continuously.

SYNOP observations

SYNOP observations of 2-metre temperature and snow depth play an important role in the assessment of the impact of the new snow scheme as well as the urban model. SYNOP observations are exchanged through the WMO Global Telecommunication Service (GTS) and are used everyday for initialisation and monitoring of NWP models. The usage of in-situ SYNOP observations within the ECMWF IFS model is described in Haiden *et al.* [87].

4.3. Evaluation of updated land cover and vegetation

4.3.1. Land use/Land cover and Leaf Area Index Evaluation

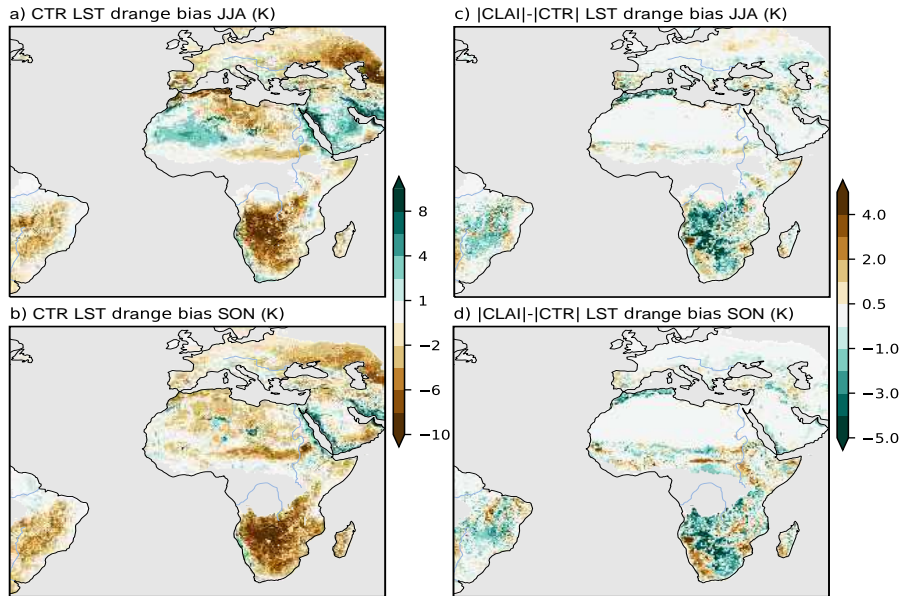


Figure 9. Mean diurnal range (drange) bias of Land Surface Temperature (LST) in the control simulation (CTR) during June-August (JJA, panel a) and September-November (SON, panel b). Difference of the mean absolute bias in the simulation with new ESA-CCI LU/LA map and LAI disaggregation (CLAI) in respect to the control simulation for JJA (c) and SON (d). Note that the color bar for differences in panels c,d has a range that is only half of the range in panels a,b. The statistics were computed for the period 2004 to 2015 considering only clear-sky conditions.

Evaluation of the new ESA-CCI LU/LC map and LAI disaggregation operator is performed through global offline and forecast coupled simulations. The offline simulations are driven by ERA5 meteorological data. A control simulation (CTR) with the current operational maps is compared with a simulation that includes the new ESA-CCI LU/LC map and the new LAI disaggregation operator (CLAI). The impact of the changes in LU/LC and LAI are assessed by evaluating the mean diurnal range of Land Surface Temperature (LST). The simulations are compared with the (LSA-SAF) LST. For each day and pixel, when at least 75% of the 3-hourly data was available the daily maximum and minimum LST are extracted to compute the diurnal range (representing the amplitude of the diurnal cycle) and the evaluation is performed for different seasons for the period 2004-2015. The mean LST diurnal range bias of the control simulation during June-August (JJA) and September-November (SON) for the 2004-2015 period is shown in Figure 9a,b. These two seasons were selected due to the high coverage of clear-sky conditions in the MSG disk, but the main features of the biases are similar in the remaining seasons. In both seasons there is wide-spread and substantial under-estimation of the diurnal range, which can reach values larger than 6 K in several regions such as the Iberian Peninsula, Southern Africa and East South America. During JJA there are indications of an over-estimation of the diurnal range in West Sahara and the Arabian Peninsula (Figure 9a). However, in these two regions there are some concerns on the quality of the LST satellite retrieval due to contamination by aerosols

(West Sahara) and emissivity directional effects (Arabian Peninsula). The change in mean absolute error of the mean LST diurnal range between the simulation with the new ESA-CCI LU/LC and LAI (CLAI) and the control simulation for JJA and SON are shown in panels c,d of Figure 9. The results show a general reduction of the under-estimation of the diurnal range in the CLAI simulation. The increased diurnal range in CLAI is mostly driven by higher daytime maximum LST (not shown) and are consistent with previous results that indicated the added value of the updated LC and LAI in CLAI in terms of the LST diurnal cycle. Previous studies have also explored the role of vegetation seasonality [37,88], suggesting that further improvements of the LST diurnal cycle can be achieved.

In addition to the evaluation of the LST diurnal range, the mean evaporation of the CTR and CLAI simulations are compared with two independent estimates of evapotranspiration (ET) mostly constrained by remote sensing data: (i) the GLEAM version 3b (Martens *et al.* [78]) and (ii) FluxCom Remote sensing ensemble flux products [76]. Figure 10 shows the comparison of evaporation (ET) 2003-2015 annual mean between the control run (CTR) and the CLAI run. Left panels show the CTR percentage bias ($pbias = 100(exp - obs) / obs$) with regards to GLEAM (GL3b) and FluxCom (FCRS) ET products as observation proxies (a and c panels respectively). The right panels show the absolute $pbias$ difference between the CLAI experiment and the CTR experiment, where GLEAM has been used for verification in panel (b) and FluxCom in panel (d). These differences show an overall reduction of the bias compared to both products (green colour). However, the results also show that on an annual time-scale, the improvements in $pbias$ with CLAI with respect to CTR are fairly small compared to the differences of the observational-based products. The latter is illustrated by comparing GLEAM and FluxCom in panels (a) and (c). It highlights the uncertainty in estimating ET as also confirmed in Jung *et al.* [76].

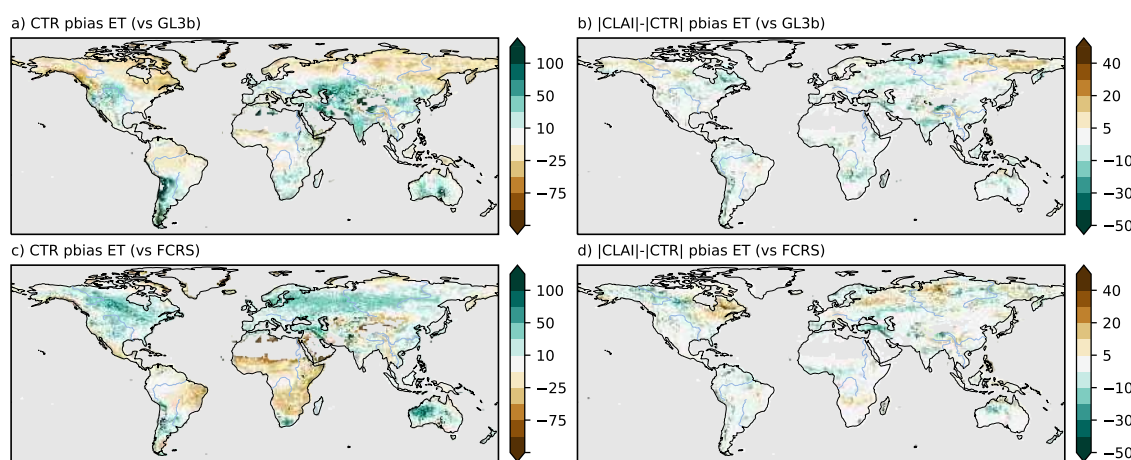


Figure 10. Annual mean evapotranspiration relative bias (%) with respect to GLEAM (a) and FluxCom (c); and the absolute relative bias difference (%) between the ESA-CCI+LAI (CLAI) experiment and the control experiment (CTR), where GLEAM is used for verification in (b) and FluxCom in (d). Note the different range of the color-bars between panels a,c (-100 to 100) and panels b,d (-50 to 50)

Evaluation of coupled forecast simulations is performed against the operational analysis. Given the different time scales between land surface processes and atmosphere, and to avoid spin-up problems related to unstable surface state, the surface initial conditions of each forecast experiments are obtained from the corresponding surface offline simulations. The focus is on short-range forecasts which have the advantage that the synoptic situation is in the predictable range. Still, changes in land cover and LAI will have an impact on near-surface atmosphere through radiative forcing and sensible and latent heat flux.

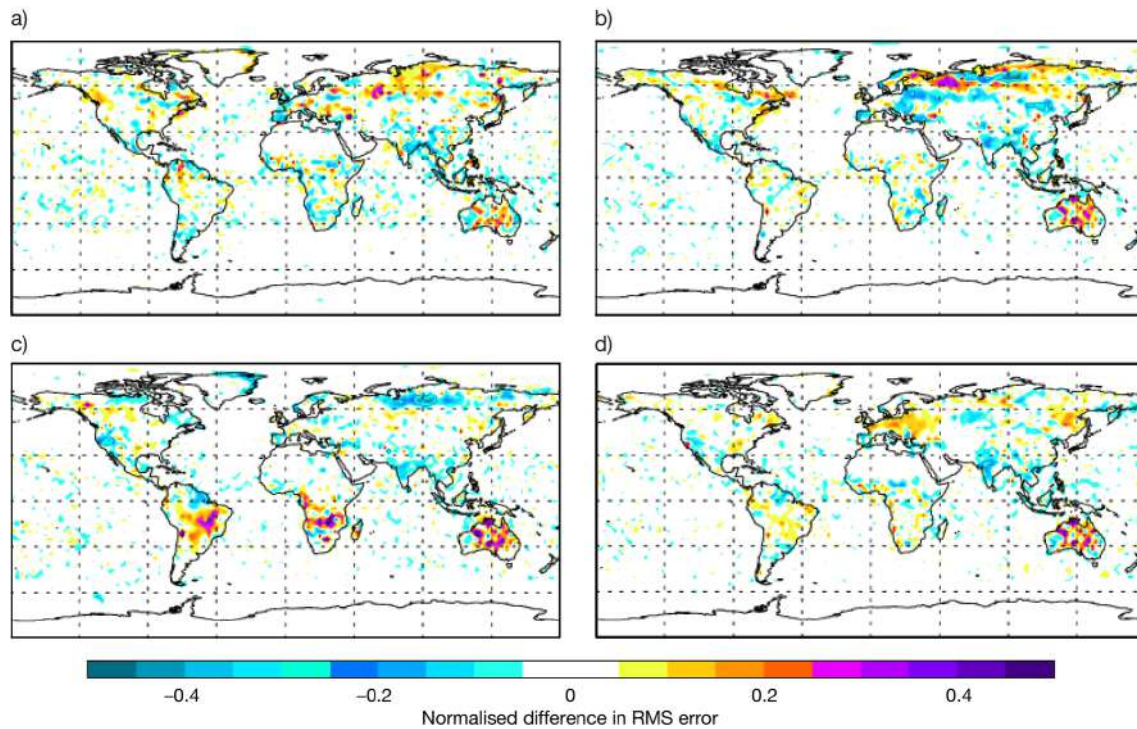


Figure 11. 2m temperature normalised RMSE difference between 36-hour forecasts using ESA-CCI LU/LC with the new LAI disaggregation operator (CLAI) and a control simulation using the operational configuration (CTR) for JF (a), MAM (b), JJA (c) and SON (d)

Screen-level temperature and dewpoint can be verified using the analysis, which draws closely to the surface synoptic observations. Figure 11 shows the 2m temperature normalised RMSE difference between forecasts based on the new ESA-CCI LU/LC map with LAI disaggregation operator and forecasts based on the current operational maps with regards to the operational analysis for the 4 seasons.

A mixed signal is seen for different areas with a marked reduction of the 2m temperature rmse (bluish colour) when using the updated vegetation especially in the northern hemisphere during MAM and JJA (panels b and c respectively), while JF and SON (panels a and d respectively) are marked with a mainly neutral impact. Although the overall results of introducing these updated vegetation maps are neutral to positive, a few areas still show a degradation in some atmospheric parameters pointing to the need for additional investigations and a parameter optimization with respect to the complex boundary layer turbulence interactions. This development is crucial for an accurate land surface representation and is therefore part of the operationally viable research for upcoming cycles.

4.3.2. Evaluation of dynamic vegetation

Seasonal vegetation cover evaluation

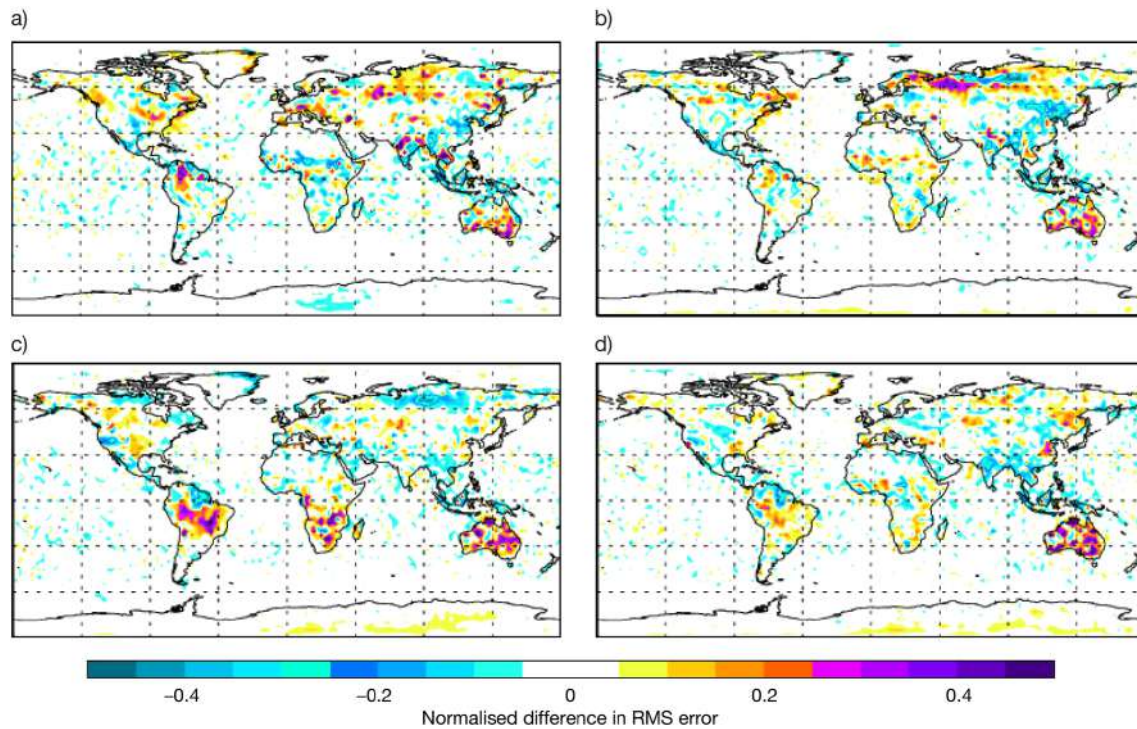


Figure 12. 2m temperature normalised RMSE difference between forecasts using the seasonal vegetation cover (FSCV) and the control simulations with static vegetation cover (CTR) for (a) DJF, (b) MAM, (c) JJA and (d) SON

The vegetation cover seasonality is also evaluated with global offline and forecast coupled simulations. Figure 4 (b) shows low vegetation cover difference between January and July when using a clumping based seasonality. This is in contrast with the current static vegetation cover field, which has the same vegetation cover all year round. Figure 4 (a) shows the difference of the seasonal bareground cover for July as compared with the current static map. This variability in cover impacts the global circulation as it is directly linked with the surface roughness. Moreover it affects surface albedo especially in winter and spring during the snow season e.g. through the shading of snow under high vegetation with a strong impact on energy fluxes. This configuration is also assessed in Nogueira *et al.* [88] and showed an overall bias reduction of the maximum LSA-SAF LST with some scattered deterioration, especially in south America which was attributed to a misrepresentation of land use related parameters. In the forecast experiments, this change is tested on top of the previous ESA-CCI+LAI (CLAI) configuration. The impact on the near surface parameters in this case also showed mixed patterns which tend to amplify both positive and negative signals found when using the CLAI configuration only. Figure 12 illustrates the 2m temperature normalised RMSE difference between the coupled forecast simulations based on the seasonal vegetation cover (FSCV) and the simulation based on the current operational static cover map (CTR). The operational analysis for the 4 seasons is used as a proxy for observations. The mixed signals in the verification emphasize that vegetation changes are not independent of other model settings which often require further optimisation of vegetation related parameters such as roughness length, vegetation minimum stomatal resistance and the surface skin conductivity. They all modulate the exchanges between the surface and the atmosphere and point to the need to further adjust this development as operationally viable for future cycles.

Prognostic vegetation phenology evaluation

The prognostic phenology evaluation is performed with offline in-situ and offline global simulations driven by ERA-Interim forcing. A relaxation coefficient r_B (eq. 3) of 0.05 day^{-1} was

used in this case. The results show that this simple growth model is able to detect growth anomalies with regards to a multi-year climatology. Figure 13 illustrates the above ground anomaly index (AI_{AGB}) for November 2010 with regards to the 1999-2013 climatology defined as

$$AI_{AGB} = \frac{AGB_{Nov2010} - AGB_{CLIM1999-2013}}{AGB_{CLIM1999-2013}} \quad (5)$$

November 2010 is chosen because it is characterized by a drought in the Horn of Africa and a wet event corresponding to drought recovery in central and eastern Australia. Given the tight link assumed in this parametrization between the above ground biomass and LAI, this map correlates well with both Copernicus global land (CGLS) observation-based and simulated LAI anomaly maps of the same period (not shown). In the Horn of Africa, the above-ground biomass can be less than 20% of the 15 year mean ($AI_{AGB} < -80\%$), while for the Australia wet case, the anomaly is positive and in some areas it exceeds the 15 year mean by 60%.

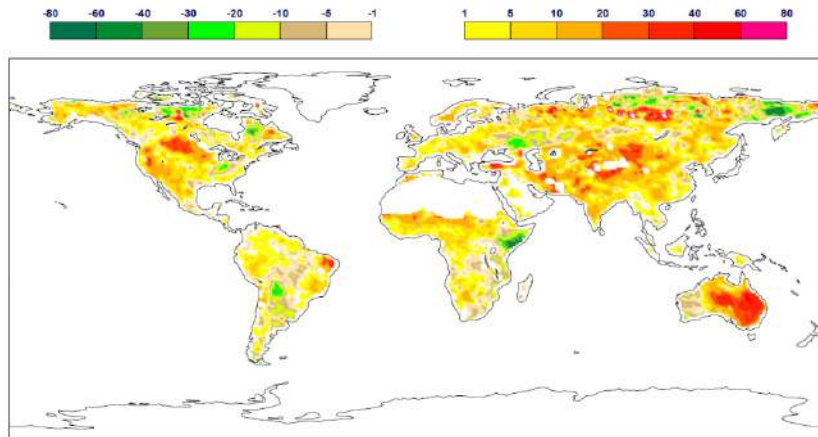
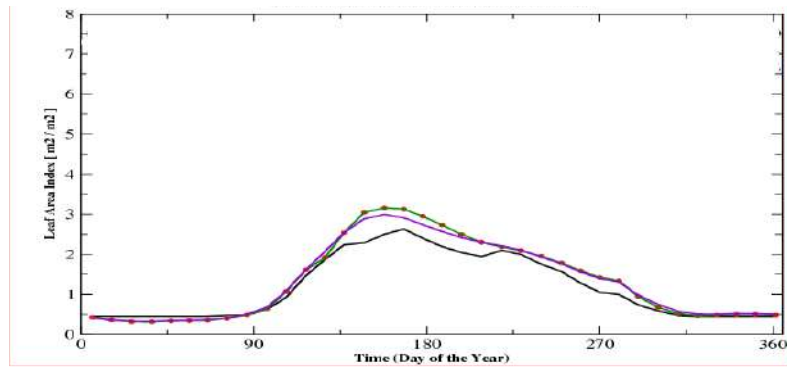


Figure 13. Above ground biomass-based Anomaly Index (AI_{AGB}) for November 2010 in % of the 1999-2013 mean.

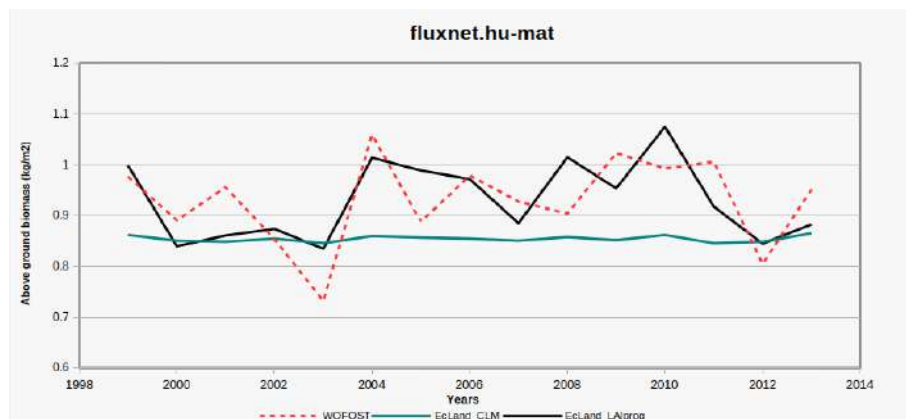
The in-situ evaluation is performed with the Flux tower network (FLUXNET) data (Baldocchi *et al.* [79]) and the World Food Studies (WOFOST) products which are currently developed by the Crop Growth Monitoring System (CGMS) within the Monitoring Agricultural Resources unit (MARS) of the European Joint Research Centre (JRC).

Figure 14 is an illustrative example of this evaluation, where Figure 14a shows that the growth model reasonably simulates the LAI (black line) as compared to both the observed LAI (near real time Copernicus Global land LAI product GEOV1) and its corresponding 1999-2013 climatology (purple line). Although it slightly underestimates its maximum value for the considered Hungarian site (hu-mat), the correlation with the near real time LAI is slightly improved.

In this case, for 2004 at hu-mat site, the gross primary production (GPP) based on prognostic LAI correlates better ($r = 0.925$) with smaller RMSE ($RMSE = 1.105$) than when using the GEOV1 LAI ($r = 0.894$, $RMSE = 1.260$). The time series of the above-ground biomass (AgB) from 1999 to 2013 for the Hu-mat site is illustrated in 14b. It shows that using the growth model (black line), the AgB correlates much better with the WOFOST products than when using the prescribed LAI climatology. These results are indicative of the overall impact of the growth model at the site level, although for other sites (not shown) the impacts may fluctuate. It should be noted here that this development is not implemented in coupled forecast mode and therefore still requires further testing to be included in the operational system.



(a) Observed LAI in m^2/m^2 for 2004 at Fluxnet Hu-mat station (green with red dots), LAI climatology (purple), and prognostic LAI (black)



(b) Above-ground biomass in kg/m^2 from WOFOST (red), ECLand with climatological LAI (green) and ECLand with prognostic LAI (black)

Figure 14. In-Situ evaluation of the vegetation related variables when using the growth model.

4.4. Evaluation of updated snow

The new multi-layer snow scheme has been evaluated in offline simulations forced with observed meteorological data from the ESM-SnowMIP network [89], as well as in global offline simulations driven with ERA5 forcing data and in coupled ocean-land-atmosphere forecasts.

Site evaluation at ESM-SnowMIP

Figure 15 shows summary statistics for Snow Water equivalent (SWE) and snow depth (SD) using the SL and ML5 snow schemes, evaluated at the ESM-SnowMIP sites. ML5 improves the bias, correlation and standard deviation of the errors at most of the sites considered. The largest improvements are found at Col de Porte (cdp), as reported already in Arduini *et al.* [41]. Senator Beck (snb) is the only site showing a consistent degradation in both SWE and SD, for which both correlations and errors increase for ML5 [see 41, and discussion therein]. SL has an overall positive bias in SWE and SD at most of the ESM-SnowMIP sites, at some sites exceeding 20%. ML5 generally reduces the biases, changing sign (negative) at some sites.

The impact of the new vertical discretisation on mountain sites is shown in Fig. 16, by comparing a simulation at the Swamp Angel site with and without the snow depth-dependent vertical discretisation over complex terrains. The latter configuration, called ML5-noOro, corresponds to a simulation with the same vertical discretization of the snowpack as used by Arduini *et al.* [41]. ML5-noOro shows an overestimation of melting during the end of the snow season in particular years, which is alleviated in ML5. Considering the entire time period, the impact over mountain sites of the new parametrization is

generally positive (not shown).

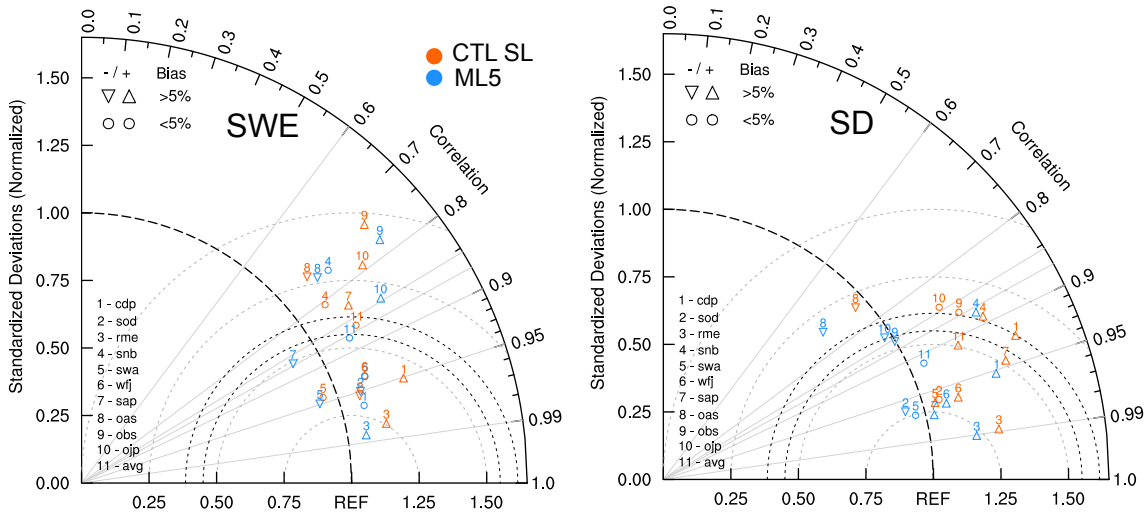


Figure 15. Taylor diagram of Snow Water Equivalent (SWE, left) and snow depth (SD, right) for offline simulations using the single-layer (CTL SL, red) and multi-layer (ML5, blue) snow schemes over the ESM-SnowMIP sites; see Sect.4.2 for details on the ESM-SnowMIP sites.

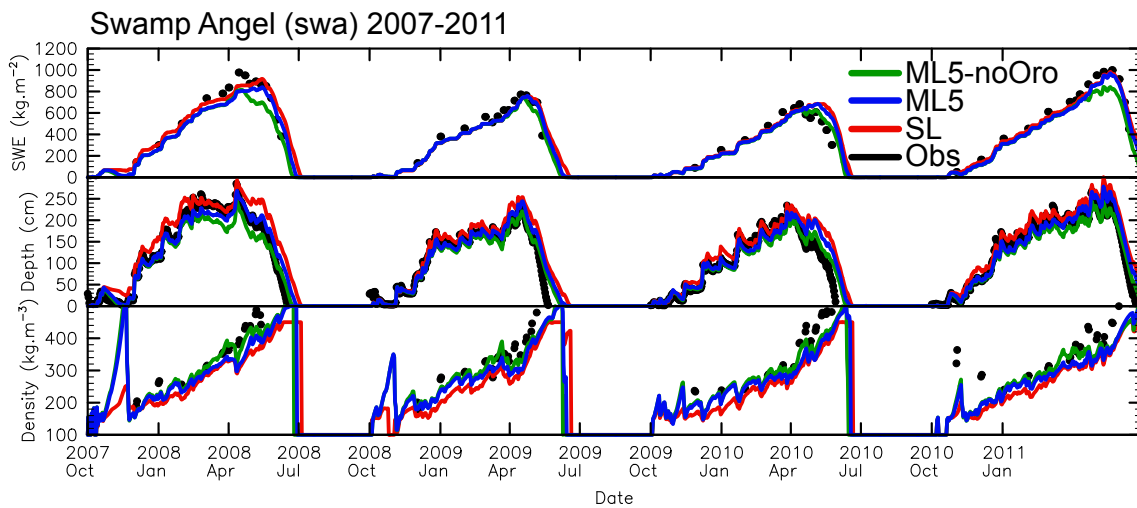


Figure 16. Time series of snow water equivalent (SWE), snow Depth, and snow Density for Swamp Angel (swa) from observations (Obs, black dots) and the offline experiments using the single-layer (SL, red lines), multilayer (ML5, blue lines), and multilayer without the snow depth-dependent snow layer thickness described in Sect. 3.3.1 (ML-noOro, green lines). The latter configuration corresponds to a simulation with the same vertical discretization of the snowpack as used by Arduini *et al.* [41].

Global offline evaluation of the snow depth

The synoptic observations of snow depth on the Global Telecommunication System (GTS), which are routinely assimilated in the ECMWF snow analysis [90], are used to evaluate global offline simulations with the multi-layer (ML5) and single-layer (SL) snow schemes. The evaluation period covers the months between fall to spring (September to May) from 2014 to 2018. Figure 17 shows a general reduction of the root-mean-square error (RMSE) of snow depth when using the multi-layer snow scheme, with the largest improvements over North America and complex terrain regions. Analysis of the error distribution shows a reduction of the median value of the bias and RMSE, and generally an improvement at stations characterized by the largest errors (see Fig. 17b).

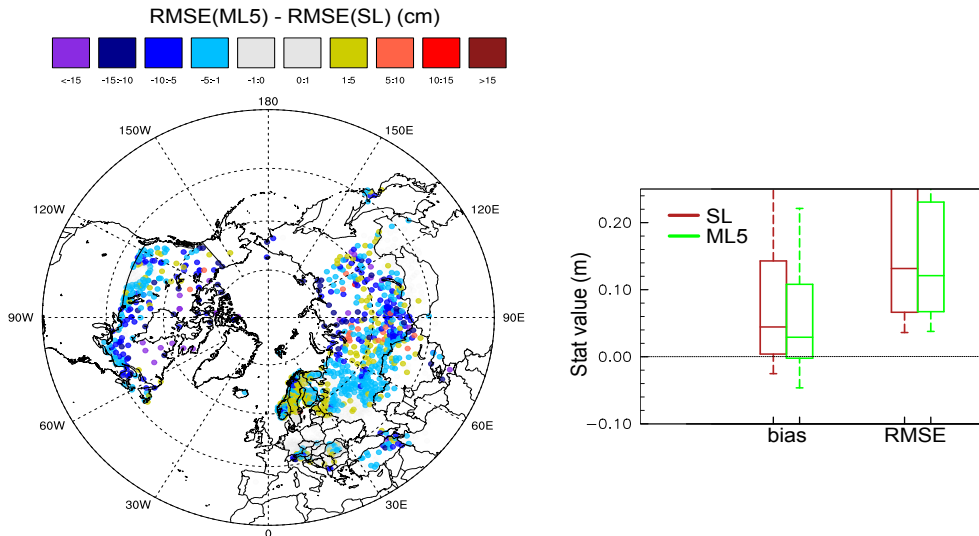


Figure 17. Left: RMSE difference of snow depth between global offline simulation using the multi-layer (ML5) and single-layer (SL) snow schemes for December to May period from 2014 to 2018. Blue colours indicate reduced RMSE in ML5. Right: boxplot of snow depth statistics (bias and RMSE) using stations considered in Left panel.

Global coupled evaluation

Evaluation of the multi-layer snow scheme in coupled forecasts has been performed over multiple winter periods looking at the impact on weather parameters and surface fluxes using a wide range of diagnostics [41,91]. Using a thinner snow layer with a low thermal inertia enables better representation of strong cooling events occurring in snow-covered conditions, because the snow surface responds on quicker time-scales to changes in the atmospheric forcing. This leads to an increase of the amplitude of the diurnal cycle of 2m temperature over snow-covered surfaces, as well as to an increase of its variability.

Figure 18 shows the absolute mean bias and root-mean-square error differences over a winter period (DJF) between coupled forecasts at a lead time of 2 days using the multi-layer snow scheme and the current single-layer snow scheme. 2-metre temperature observations from the synoptic station network, used routinely in the ECMWF assimilation system for monitoring and diagnostics, are used as a benchmark.

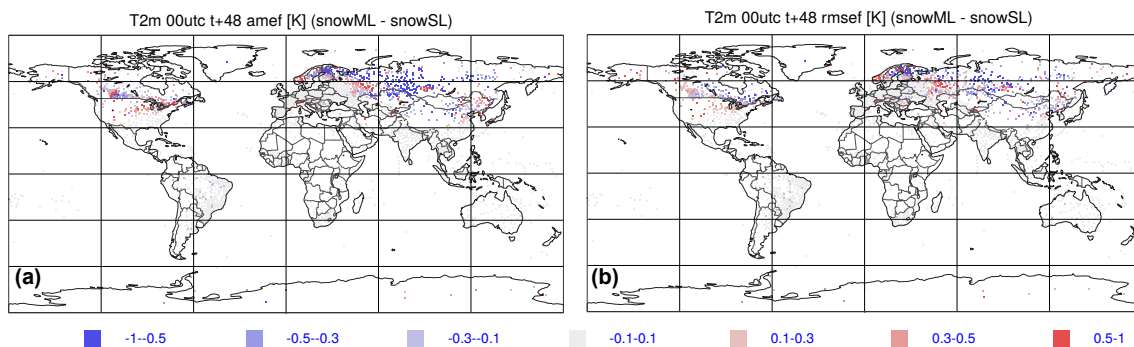


Figure 18. Temperature verification at screen level (T2m). (a): Absolute mean error difference (amef) at a lead time of 2 days between coupled forecasts with the multi-layer (snowML) and single-layer (snowSL) snow schemes; (b) Same as (a), but showing root-mean-square-error difference (rmsef).

Results indicate a reduction of the mean error in particular in the high-latitude regions, which can be associated to an improved prediction of very cold temperatures over snow-covered regions. The RMSE of T2m is reduced in the snow multi-layer forecasts over most of Eurasia regions, however it increases over certain regions, for instance in Alaska and West Scandinavia. This can be partly

associated to errors in other variables and processes, like cloud cover and/or cloud microphysics, for which the new scheme is more exposed [more “responsive”, as described in 41]. However, the increase of RMSE over complex terrain can be also related to an increase of the preexisting biases in the control forecasts, which can be partly due to the relatively low horizontal resolution used in these experiments (25 km). The increase in variability can be advantageous in a probabilistic framework, through the increase in forecast spread [92]. The overall results of the updated snow scheme indicate its readiness for implementation in the next operational cycle.

4.5. Evaluation of updated soil parametrization

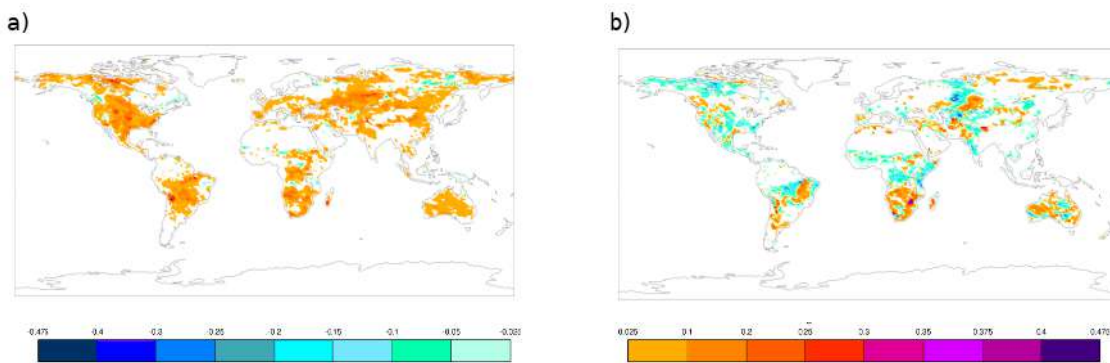


Figure 19. Difference in correlation with FluxCom energy fluxes between the 10-layers soil experiment (OSML10_TW) and the standard 4-layers experiment (a) Sensible heat flux (b) Latent heat flux

The updated soil depth and vertical discretization is assessed with surface offline simulations forced with ERA5. A control simulation with the default 4 layers and 2.89m depth is compared with 2 additional configurations; one using a 10-layer/8m depth configuration for both water and temperature (OSML10_TW) and in the other, the depth is only extended for temperature while keeping the default 2.89m depth for water (OSML10_T). Evaluated against the FluxCOM energy flux products, both 10-layer configurations show different signals for the latent and sensible heat fluxes compared to the control standard 4-layers configuration. As an illustrative example, Figure 19 shows that using the 10-layer configuration results in an increase of the sensible heat flux correlation with the FluxCOM product compared to the standard 4-layer configuration, while the latent heat flux shows a general decrease of the correlation with increase over arid areas. Note that in this case, the 10-layer configurations (OSML10_TW) and (OSML10_T) have very similar correlations for flux scores, although the configurations with 8m for temperature and 2.89m depth for water has different patterns in subsurface runoff (figures not shown).

Following the evaluation of the Land Cover and LAI impact on the diurnal range of LST (see Figure 9, the impact of the increased vertical resolution in the soil is also assessed by evaluating the LST diurnal range. Figure 20 shows the absolute bias difference of the mean diurnal range of LST between the OSML10_TW simulation and the control simulation for JJA (top panel) and SON (bottom panel). Similarly to the reduction of the diurnal range underestimation seen in CLAI (Figure 9), the increased vertical resolution of the soil near the surface also reduces the diurnal range under-estimation over the Iberian Peninsula, South Africa and Eastern South America. In general, the increased vertical resolution drives an increase of the LST diurnal range, due to a reduction of the thermal inertia of the top soil layer. While this compares favourably in most of the MSG disk, in the Western Sahara and Arabian peninsula there is an increase of the bias during June-August (Figure 20a) and in SON over the Arabian peninsula (Figure 20b). This is consistent with the already existing over-estimation of the diurnal range in the control simulation, which is likely associated with limitations of the LSA-SAF product in those regions due to Aerosols (West Sahara) and directional effects (Arabian Peninsula).

Both changes in land cover, LAI and vertical resolution in the soil show a positive impact on the LST diurnal range. Further research is needed to understand if these two are additive and to assess the benefits (and limitations) of these two changes in the representation of the LST diurnal cycle.

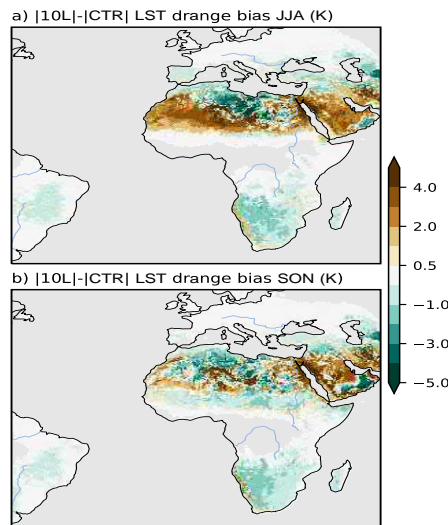


Figure 20. Difference in absolute mean diurnal range (drange) bias of Land Surface Temperature (LST) between the simulation with OSML10_TW (10L) and the control (CTR) simulation for JJA (a) and SON (b). The statistics were computed for the period 2004 to 2015 considering only clear-sky conditions. The biases of the control simulation are shown Figure 9

The impact on soil moisture is evaluated with the ESA-CCI soil moisture product (Gruber *et al.* [83], Dorigo *et al.* [84] and Gruber *et al.* [85]). Figure 21 shows the difference of the surface soil moisture correlation with regards to the ESA-CCI surface soil moisture product between simulations using the 10-layer configuration and the current 4-layer configuration for JJA 2018. It is shown that during dry season, the surface soil moisture of the 10-layer configuration correlates better with the ESA-CCI soil moisture as the satellite observation depth matches better the surface layer depth of the 10-layer configuration.

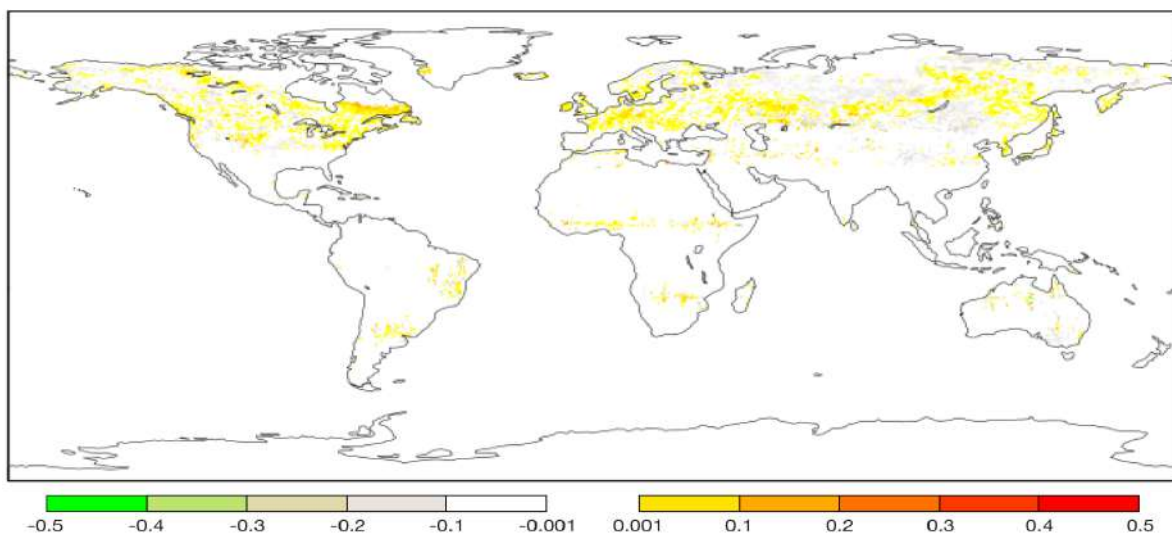


Figure 21. Difference of the surface soil moisture correlation with regards to the ESA-CCI surface soil moisture product between simulations using the 10-layer configuration and the current 4-layer configuration for JJA.

With the coupling with the river discharge model (section 4.7), and the possibility brought with the hydrological verification, this development would benefit from additional constraints for uncertain or non-observable model parameters related to soil hydrology which would facilitate its operational implementation. The estimation of these uncertain model parameters would even be facilitated and automated once the multiscale parameter regionalization system (MPR, [93]) is fully coupled with ECLand. This development would be then viable for operational implementation in the upcoming cycles.

4.6. Evaluation of the updated surface water

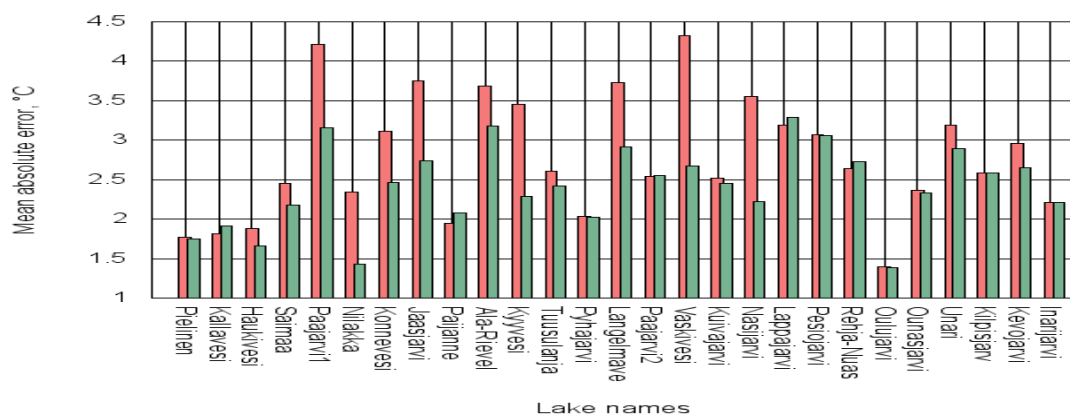


Figure 22. Lake temperature mean absolute error for 27 in-situ Finnish lakes over the 2010–2014 period. Results for the current operational system are in red and results with the updated lake depths are in green.

Modelled lake surface temperatures were verified against in situ measurements recorded by the Data and Information Centre of the Finnish Environment Institute (SYKE) over 27 lakes for 2010–2014. In situ lake water surface temperatures are measured every morning during the ice-free season at 8 am local time, close to the shore, at 20cm below the water surface [53]. The model values from offline surface experiments forced with ERA5 were sampled to correspond to the measured values (i.e. during ice-free season at 5:00 or 6:00 UTC depending on daylight saving time).

An overall error reduction is seen in Figure 22. With a more realistic lake depth, the mean absolute error from 2010 to 2014 becomes smaller for nearly all lakes. Averaged over all 27 lakes a 13.4% error reduction is achieved. For some lakes, the water temperature modelling errors remained the same as their depth values are the same or nearly the same. These lakes are Paijanne, Pyhajarvi, Paajarvi2, Kuivajarvi, Pesiojarvi, Rehja-Nuas, Kilpisjarvi and Inarjarvi. The only statistically significant deterioration in the temperature scores was for Lappajarvi, whose depth is overestimated 2.5 times in the updated depth file (18.0m instead of 6.9m) due to the depth mapping algorithm and/or horizontal resolution of the depth field.

The updated land/water water maps are planned for implementation in the ECMWF IFS operational system, as it will reduce uncertainties related to such ancillaries. In this case the evaluation is performed based on data assimilation experiments with subsequent daily forecasts. The near surface temperatures are shown in figure 23. The simulations were performed for 2020 winter and 2019 summer seasons. RMS errors of daily 24 and 36 hour forecasts are computed with respect to the own analysis at the corresponding verification time. Figure 23 shows the 2m temperature RMSE difference, normalised by rmse, between the forecast simulations based on the new land/water maps and simulations based on the current operational maps. An overall neutral signal is seen globally for both day and night ranges (t+36 and t+48) during the northern hemisphere Winter season (Figure not shown). Summer is characterised with a neutral to positive impact (Figure 23). Locally, a slightly negative impact is seen over the Canadian Northern coast and a positive signal marked with a reduction of the 2m temperature

RMSE when using the updated land/water maps over Greenland. These impacts correspond to the differences of land/water points seen in figure 7. The overall evaluation shows that the IFS would benefit from a more accurate surface water representation and it is therefore considered for operational implementation in the next cycle.

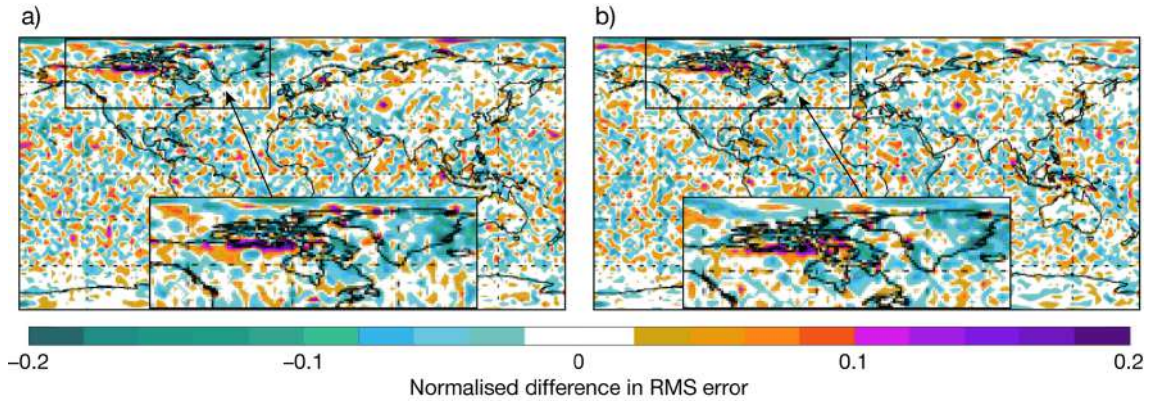


Figure 23. 2m temperature normalised root mean square error (RMSE) difference for northern hemisphere Summer between 4dvar simulations with the updated surface water map and the current operational version. The error differences refer to 36-hour (a) and 48-hour (b) forecasts initialized at 0UTC.

4.7. Evaluation of coupled river discharge

The evaluation of river discharge in different configurations is presented in Figure 24. The main goal of these results is to illustrate the different capabilities of the system for various applications. The evaluation displays the distribution of the temporal correlation and percent bias of daily river discharge for several stations on the Mackenzie (panels a,b) and Danube (panel c,d) basins, with the number of stations listed on the top of each panel. The observations are taken from the Global Runoff Data Centre (GRDC). All simulations were carried out at the $1/4^\circ$ resolution for CaMa-Flood and TL639 for ECLand (same resolution as ERA5, about 32km) extending since 1979 to 2018, and the evaluation is performed between 1982 and 2018 considering the available station data with at least 5 years of daily data. The boxplots in each panel show the distribution of the correlation and percent bias for 6 configurations. “coup1” is the default 1-way coupling with ECLand driven by ERA5 near-surface meteorology. “coup2” is a 2-way coupling simulation allowing water extraction from floodplains and update of inland water fraction in ECLand following CaMa-Flood flooded area extent. “iner” and “kine” are two stand-alone CaMa-Flood simulations driven by the runoff of “coup1”, differing in the flow velocity calculations in CaMa-Flood, using the local inertia in “iner” (the default configuration) and the kinematic wave in “kine”. Finally, “era5” and “era5l” are also stand-alone CaMa-Flood simulations driven by the runoff of the reanalysis ERA5 and ERA5-Land, respectively.

The results in Figure 24 show a neutral impact on river discharge simulation of the 2-way coupling, when compared with 1-way coupling on the selected basins. This is expected as both basins do not have large flooded areas. Results on some stations in the Amazon basin show some impact but reduced (not shown). However, the 2-way coupling configuration is still experimental and further developments are necessary for a consistent 2-way coupling, in particular on the handling of grid-scale versus sub-grid scale inland water in ECLand. The CaMa-Flood stand-alone configuration iner, shows identical results to coup1, as expected. The kinematic solution for flow velocities (kine) has some impact on the temporal correlations, with mixed results in the two analyzed basins. The local inertia solution is more accurate for large upstream areas where small water level slopes dominate the river flow, and is of particular relevance in representing surface water elevation. In smaller upstream regions with higher terrain slopes both local inertial and kinematic wave solutions are similar, with a reduced computational cost for the kinematic wave solution. Therefore, for particular applications

were computational cost is relevant (e.g. ensemble forecasting) this could be considered. Finally, the flexibility of driving the hydrodynamic component with different runoff inputs is illustrated with the results of using ERA5 and ERA5-Land (era5 and era5l simulations in Figure 24). The era5l simulations are very close to coup1 (and iner) as the main difference is the spatial resolution of the runoff fields produced by ECLand (9km in the case of era5l and 35 km in coup1/iner). Larger differences appear in era5, in particular for the percent bias (panels b,d 24). These are associated with the soil moisture and snow mass increments of the land data assimilation in ERA5 that changes the land surface water balance [56]. As previously mentioned, the full operational integration of CaMa-Flood in the IFS will be possible in future cycles with additional developments for distributed memory parallelism in CaMa-Flood and for coupling of river discharge with the ocean model.

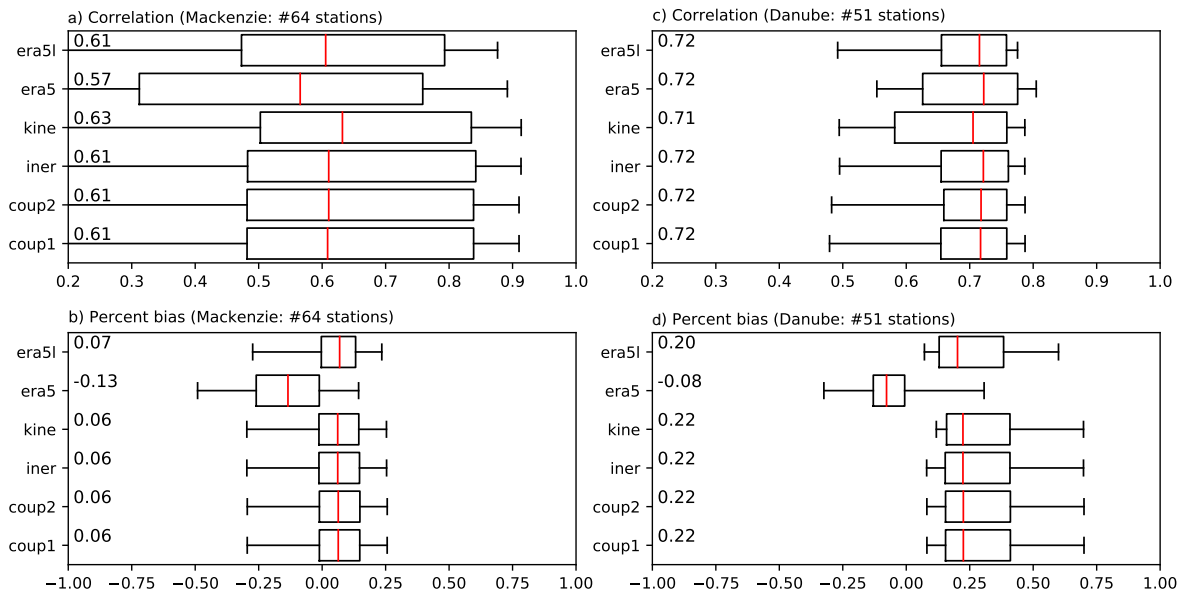


Figure 24. River discharge evaluation distribution of several stations in the Mackenzie (a,b) and Danube (c,d) basins. The evaluation is performed on daily data, displaying the distribution of correlation (a,c) and percent bias (b,d) of several model configurations (vertical axis): coup1: 1-way coupling between ECLand and CaMa-Flood; coup2: 2-way coupling between ECLand and CaMa-Flood stand-alone simulations with the flow velocity calculations using the local inertia solution (iner) and kinematic wave (kine), both driven by runoff from coup1. era5 and era5l are also stand-alone CaMa-Flood simulations driven by the runoff of ERA5 and ERA5-Land reanalysis, respectively. The boxplots whiskers extend from percentiles 5 to 95, with the box representing percentiles 25 and 75 and the median in red. The values displayed on the left, close to the vertical axis, identify the median value for each distribution.

4.8. Evaluation of urban representation

The evaluation of the single-layer urban scheme has been performed using both the IFS single-column model and ECLand. Urban parameters were first optimised with the IFS single-column model using a Gauss-Newton non-linear least square algorithm and observations of 2m temperature from 8 European surface sites. The surface albedo, emissivity, volumetric heat content and thermal conductivity were simultaneously optimised for average urban roofs, roads and walls. Monthly comparisons with hourly output for independent (January) observations show model improvement when using the urban scheme at all sites except Warsaw (Figure 25). The Warsaw site is at an airport located outside of the city, which does not provide a realistic representation of an urban environment. When using the urban scheme, the largest temperature changes occur in summer at night with smaller changes in the daytime (Figure not shown). These changes typically agree well with observation based studies, which also find urban heat island enhancements are larger at night than during daytime ([94]; [95]).

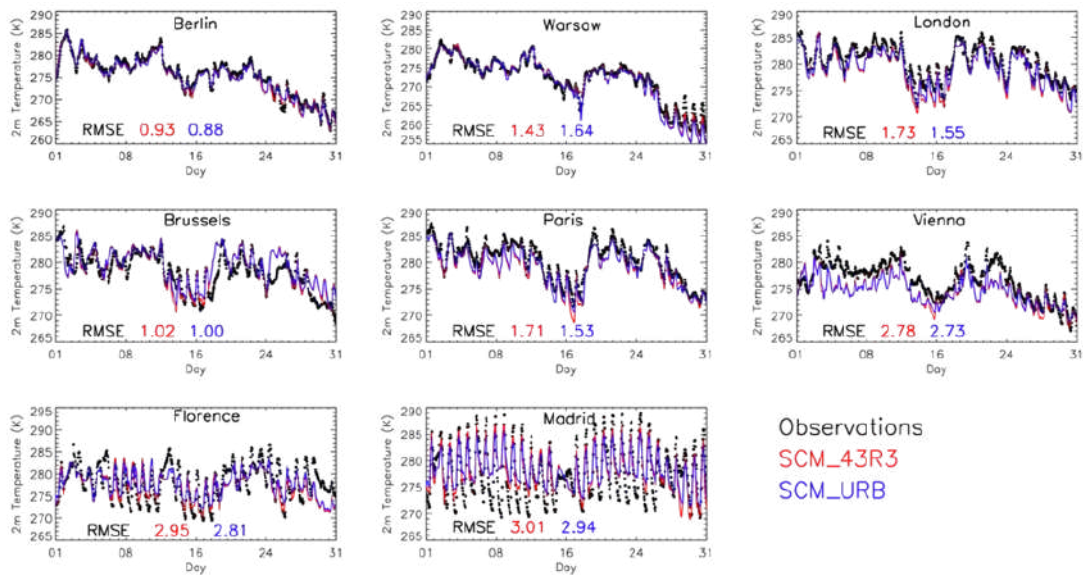


Figure 25. Hourly observed 2m temperature taken from 8 urban sites for January 2012 (black circles). Also shown are single-column model results using the control model (SCM_43R3: red) and the optimised urban scheme (SCM_URB: blue). Numbers indicate RMSE values when compared to observations. (Adapted from [72])

High-resolution global ECLand simulations (~1 km horizontal) show expected skin and 2m temperature enhancements over both large and small urban conurbations (Figure 26). At coarser resolution the signal from smaller conurbations is lost (~9 km) and a small urban signal averaged over an unrealistically large area is simulated at even coarser resolutions (~30 km). It is therefore recommended that a reasonable land surface representation using the single-layer urban canopy model is only derived at resolutions of 9 km or higher. This development shows promising results to be considered as operationally viable for future cycles.

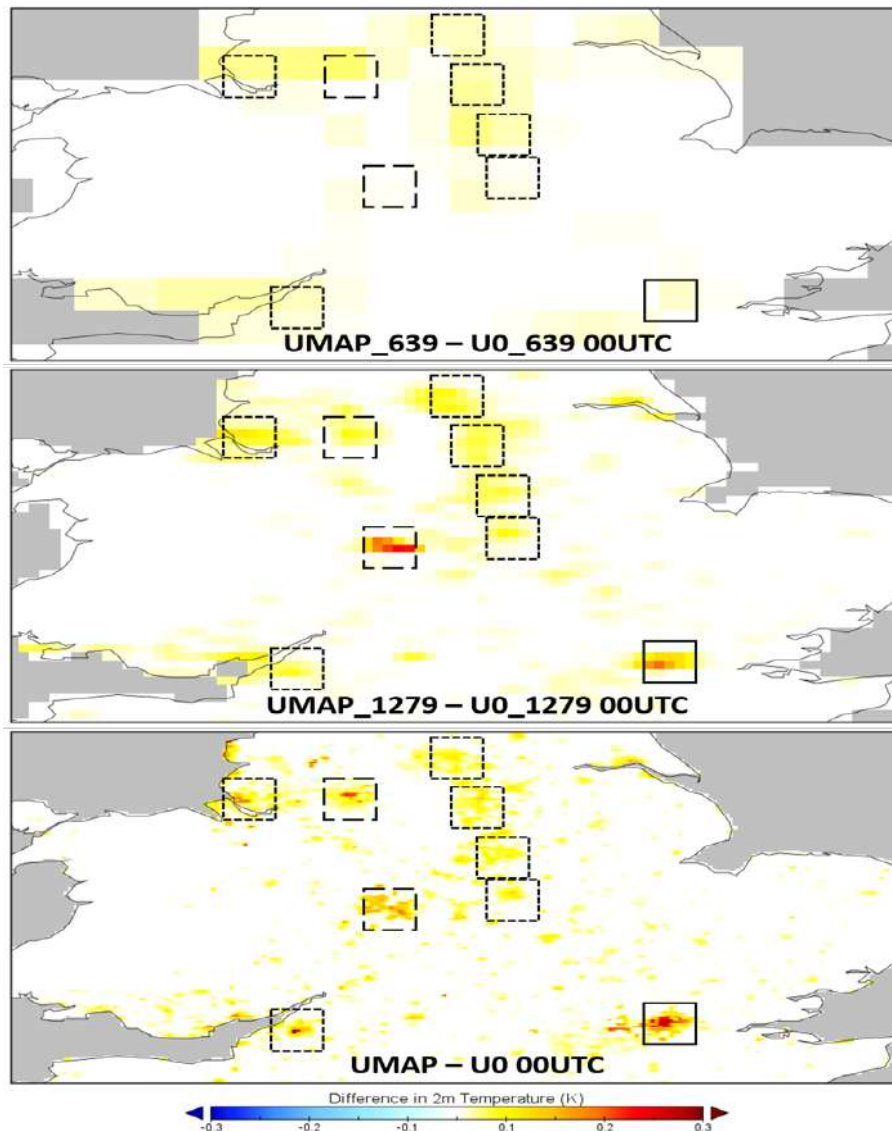


Figure 26. The difference between urban and control monthly mean 2m temperature over central UK for 00:00 UTC January 2019 at ~ 30 km (top), ~ 9 km (middle) and ~ 1 km horizontal resolution (bottom) taken from ECLand simulations. Conurbations larger than $1,000\text{km}^2$ (solid), 500km^2 (dashed) and 100km^2 (dotted) are denoted with boxes. (Adapted from [72])

5. Summary

The ECLand land-surface modelling system aims to expedite progress in Earth system modelling and greatly benefits from international collaboration by co-developing and facilitating modular extensions. ECLand is based on the Carbon-Hydrology Tiled Scheme for Surface Exchanges over Land in its current operational version (CY47R1) and represents an integral part of the IFS for ECMWF's current and future global weather and environmental (services) applications.

The paper highlights examples of recent developments in different components of the land surface model, namely : (i) vegetation, (ii) snow, (iii) soil, (iv) open water/lake (v) river/inundation (vi) urban areas, which are illustrated and evaluated against benchmark observational datasets. Future developments on the seamlessness of the land surface system target the improvement of processes affecting also the seasonal range and reanalyses, e.g. through consideration of the vegetation status inter-annual variability as also depicted in [26].

Perspectives for NWP are focusing on improvements of the water cycle, with particular attention to evaporation processes, transition seasons, hydrological forecast skill and with a focused attention to a better exploitation of emerging very-high resolution observational datasets (eg. SENTINEL), skin temperature over land with consideration to its compensating error-free interpretation. On the snow and soil perspectives, the multi-layer approach available in ECLand for snow and soil moisture opens avenues for enhanced forward modelling of satellite radiances which will enable developments of coupled assimilation of surface sensitive observations. Preliminary investigations were conducted by Hirahara *et al.* [96] showing that low frequency microwave emissivity is better represented when a multilayer snowpack model is used.

In the near future, the very high resolution modelling capabilities available with ECLand are planned to be extended to land data assimilation, using Sentinel satellites for soil moisture and snow analysis, as well as skin temperature and vegetation variables, for land reanalysis and NWP applications. Land-atmosphere coupling development priorities have been defined [26] along with ways to verify model improvements using super-sites, as well as the standard observations used in ECMWF verification activities [97]. In addition, coupling with the river discharge model will add further constraints on uncertain model parameters and would enable investigation of coupled assimilation of inland water level information in ECLand for the benefit of river discharge and land surface processes modelling. Preliminary work using the uncoupled river/IFS system showed that SMOS data assimilation has an impact on river discharge forecasts [98]. The nature of physically based models is by default attached to uncertainties coming from non-fully adequate equations for different reasons such as scale representativeness or even non-observable parameters. Ongoing collaborative efforts in ECLand are also focused on the refactoring of the land surface model to externalize process-sensitive parameters and attach the multiscale parameter regionalization system (MPR; [93]) to the offline system in order to enable more flexible parameter estimation and optimization. AI/Machine learning techniques could also be considered in this context.

Finally, enhanced vegetation and photosynthesis modelling, as well as very-high resolution modelling including anthropogenic elements such as urban, CO₂ and CH₄, and prognostic fire modelling are important elements of ECLand extensions to support current and future Copernicus services.

Future developments focus also on preserving the seamlessness of the land surface system through the improvement of the processes affecting the extended range and reanalysis, such as the consideration of the vegetation status and its inter-annual variability for upcoming C3S seasonal and reanalysis systems. This effort would be consolidated by the foreseen improved estimation and characterisation of the carbon cycle components especially the biogenic, contributing to the CAMS services.

Acknowledgments: We would like to extend our thanks to the pioneers and the different contributors to the ECMWF land surface modeling efforts: Pedro Viterbo, Bart van den Hurk, Andrea Manrique-Sunen, Annika Nordbo, Clement Albergel, Lionel Jarlan, Sebastien Lafont, Jean Christophe Calvet, Isabel Trigo, Cor Jacobs, Andrea Alessandri, Anne Verhoef, Paul Dirmeyer, Rui Salgado, Victor Stepanenko and Dmitrii Mironov for their valuable development contributions. We thank Andy Brown, Florian Pappenberger, Richard Engelen for their support and fruitful comments on the manuscript. We also thank Anabel Bowen for her help improving the figures. This work used eddy covariance data acquired by the FLUXNET community and in particular the Hu-mat site data provided through the ImagineS FP7 project. The WOFOST data was also provided through the ImagineS FP7 project by the European Joint research Centre, We thank in particular the PIs and researchers that decided to share their data freely within the scientific community.

References

1. Best, M.J.; Pryor, M.; Clark, D.B.; Rooney, G.G.; Essery, R.L.H.; Ménard, C.B.; Edwards, J.M.; Hendry, M.A.; Porson, A.; Gedney, N.; Mercado, L.M.; Sitch, S.; Blyth, E.; Boucher, O.; Cox, P.M.; Grimmond, C.S.B.; Harding, R.J. The Joint UK Land Environment Simulator (JULES), model description – Part 1: Energy and water fluxes. *Geoscientific Model Development* **2011**, *4*, 677–699. doi:10.5194/gmd-4-677-2011.
2. Clark, D.B.; Mercado, L.M.; Sitch, S.; Jones, C.D.; Gedney, N.; Best, M.J.; Pryor, M.; Rooney, G.G.; Essery, R.L.H.; Blyth, E.; Boucher, O.; Harding, R.J.; Huntingford, C.; Cox, P.M. The Joint UK Land Environment Simulator (JULES), model description – Part 2: Carbon fluxes and vegetation dynamics. *Geoscientific Model Development* **2011**, *4*, 701–722. doi:10.5194/gmd-4-701-2011.
3. Masson, V.; Le Moigne, P.; Martin, E.; Faroux, S.; Alias, A.; Alkama, R.; Belamari, S.; Barbu, A.; Boone, A.; Bouyssel, F.; Brousseau, P.; Brun, E.; Calvet, J.C.; Carrer, D.; Decharme, B.; Delire, C.; Donier, S.; Essaouini, K.; Gibelin, A.L.; Giordani, H.; Habets, F.; Jidane, M.; Kerdraon, G.; Kourzeneva, E.; Lafaysse, M.; Lafont, S.; Lebeaupin Brossier, C.; Lemonsu, A.; Mahfouf, J.F.; Marguinaud, P.; Mokhtari, M.; Morin, S.; Pigeon, G.; Salgado, R.; Seity, Y.; Taillefer, F.; Tanguy, G.; Tulet, P.; Vincendon, B.; Vionnet, V.; Voldoire, A. The SURFEXv7.2 land and ocean surface platform for coupled or offline simulation of earth surface variables and fluxes. *Geoscientific Model Development* **2013**, *6*, 929–960. doi:10.5194/gmd-6-929-2013.
4. Lawrence, D.M.; Fisher, R.A.; Koven, C.D.; Oleson, K.W.; Swenson, S.C.; Bonan, G.; Collier, N.; Ghimire, B.; van Kampenhout, L.; Kennedy, D.; Kluzek, E.; Lawrence, P.J.; Li, F.; Li, H.; Lombardozzi, D.; Riley, W.J.; Sacks, W.J.; Shi, M.; Vertenstein, M.; Wieder, W.R.; Xu, C.; Ali, A.A.; Badger, A.M.; Bisht, G.; van den Broeke, M.; Brunke, M.A.; Burns, S.P.; Buzan, J.; Clark, M.; Craig, A.; Dahlin, K.; Drewniak, B.; Fisher, J.B.; Flanner, M.; Fox, A.M.; Gentine, P.; Hoffman, F.; Keppel-Aleks, G.; Knox, R.; Kumar, S.; Lenaerts, J.; Leung, L.R.; Lipscomb, W.H.; Lu, Y.; Pandey, A.; Pelletier, J.D.; Perket, J.; Randerson, J.T.; Ricciuto, D.M.; Sanderson, B.M.; Slater, A.; Subin, Z.M.; Tang, J.; Thomas, R.Q.; Val Martin, M.; Zeng, X. The Community Land Model Version 5: Description of New Features, Benchmarking, and Impact of Forcing Uncertainty. *Journal of Advances in Modeling Earth Systems* **2019**, *11*, 4245–4287, [<https://agupubs.onlinelibrary.wiley.com/doi/pdf/10.1029/2018MS001583>]. doi:<https://doi.org/10.1029/2018MS001583>.
5. Van den Hurk, B.J.J.M.; Viterbo, P.; Beljaars, A.C.M.; Betts, A.K. Offline validation of the ERA40 surface scheme. *ECMWF Tech. Memo. No. 295* **2000**.
6. Viterbo, P.; Beljaars, A.C.M. An improved land surface parametrization scheme in the ECMWF model and its validation. *ECMWF Tech. Report No. 75* **1995**. Research Department, ECMWF.
7. Viterbo, P.; Beljaars, A.C.M.; Mahouf, J.F.; Teixeira, J. The representation of soil moisture freezing and its impact on the stable boundary layer. *Q. J. R. Meteorol. Soc.* **1999**, *125*, 2401–2426.
8. Balsamo, G.; Viterbo, P.; Beljaars, A.; van den Hurk, B.; Hirschi, M.; Betts, A.K.; Scipal, K. A revised hydrology for the ECMWF model: Verification from field site to terrestrial water storage and impact in the Integrated Forecast System. *J. Hydrometeorol.* **2009**, *10*, 623–643.
9. Dutra, E.; Balsamo, G.; Viterbo, P.; Miranda, P.; Beljaars, A.; Schär, C.; Elder, K. An improved snow scheme for the ECMWF Land Surface Model: Description and offline validation. *J. Hydrometeorol.* **2010**, *11*, 7499–7506.
10. Boussetta, S.; Balsamo, G.; Beljaars, A.; Kral, T.; Jarlan, L. Impact of a satellite-derived Leaf Area Index monthly climatology in a global Numerical Weather Prediction model. *Int. J. Rem. Sens.* **2013**, *34*, 3520–3542.
11. Uppala, S.M.; Kållberg, P.W.; Simmons, A.J.; Andrae, U.; Bechtold, V.D.C.; Fiorino, M.; Gibson, J.K.; Haseler, J.; Hernandez, A.; Kelly, G.A.; Li, X.; Onogi, K.; Saarinen, S.; Sokka, N.; Allan, R.P.; Andersson, E.; Arpe, K.; Balmaseda, M.A.; Beljaars, A.C.M.; Berg, L.V.D.; Bidlot, J.; Bormann, N.; Caires, S.; Chevallier, F.; Dethof, A.; Dragosavac, M.; Fisher, M.; Fuentes, M.; Hagemann, S.; Hólm, E.; Hoskins, B.J.; Isaksen, I.; Janssen, P.A.E.M.; Jenne, R.; McNally, A.P.; Mahfouf, J.F.; Morcrette, J.J.; Rayner, N.A.; Saunders, R.W.; Simon, P.; Sterl, A.; Trenberth, K.E.; Untch, A.; Vasiljevic, D.; Viterbo, P.; Woollen, J. The ERA-40 re-analysis. *Quarterly Journal of the Royal Meteorological Society* **2005**, *131*, 2961–3012. doi:<https://doi.org/10.1256/qj.04.176>.
12. Dee, D.P.; Uppala, S.M.; Simmons, A.J.; Berrisford, P.; Poli, P.; Kobayashi, S.; Andrae, U.; Balmaseda, M.A.; Balsamo, G.; Bauer, P.; Bechtold, P.; Beljaars, A.C.M.; van de Berg, L.; Bidlot, J.; Bormann, N.; Delsol, C.; Dragani, R.; Fuentes, M.; Geer, A.J.; Haimberger, L.; Healy, S.B.; Hersbach, H.; Hólm, E.V.; Isaksen, I.; Kållberg, P.; Köhler, M.; Matricardi, M.; McNally, A.P.; Monge-Sanz, B.M.; Morcrette, J.J.; Park, B.K.; Peubey, C.; de Rosnay, P.; Tavolato, C.; Thépaut, J.N.; Vitart, F. The ERA-Interim reanalysis: configuration

- and performance of the data assimilation system. *Quarterly Journal of the Royal Meteorological Society* **2011**, *137*, 553–597. doi:<https://doi.org/10.1002/qj.828>.
13. Hersbach, H.; Bell, B.; Berrisford, P.; Hirahara, S.; Horányi, A.; Muñoz-Sabater, J.; Nicolas, J.; Peubey, C.; Radu, R.; Schepers, D.; Simmons, A.; Soci, C.; Abdalla, S.; Abellan, X.; Balsamo, G.; Bechtold, P.; Biavati, G.; Bidlot, J.; Bonavita, M.; De Chiara, G.; Dahlgren, P.; Dee, D.; Diamantakis, M.; Dragani, R.; Flemming, J.; Forbes, R.; Fuentes, M.; Geer, A.; Haimberger, L.; Healy, S.; Hogan, R.J.; Hólm, E.; Janisková, M.; Keeley, S.; Laloyaux, P.; Lopez, P.; Lupu, C.; Radnoti, G.; de Rosnay, P.; Rozum, I.; Vamborg, F.; Villaume, S.; Thépaut, J.N. The ERA5 global reanalysis. *Q. J. Roy. Meteor. Soc.* **2020**, *n/a*, [<https://rmets.onlinelibrary.wiley.com/doi/pdf/10.1002/qj.3803>]. doi:10.1002/qj.3803.
 14. Muñoz Sabater, J.; Dutra, E.; Agustí-Panareda, A.; Albergel, C.; Arduini, G.; Balsamo, G.; Boussetta, S.; Choulga, M.; Harrigan, S.; Hersbach, H.; Martens, B.; Miralles, D.G.; Piles, M.; Rodríguez-Fernández, N.J.; Zsoter, E.; Buontempo, C.; Thépaut, J.N. ERA5-Land: A state-of-the-art global reanalysis dataset for land applications. *Earth System Science Data Discussions* **2021**, *2021*, 1–50. doi:10.5194/essd-2021-82.
 15. Weisheimer, A.; Doblas-Reyes, F.J.; Jung, T.; Palmer, T.N. On the predictability of the extreme summer 2003 over Europe. *Geophysical Research Letters* **2011**, *38*. doi:10.1029/2010GL046455.
 16. Dutra, E.; Viterbo, P.; Miranda, P.M.; Balsamo, G. Complexity of snow schemes in a climate model and its impact on surface energy and hydrology. *Journal of Hydrometeorology* **2012**, *13*, 521–538. doi:10.1175/JHM-D-11-072.1.
 17. Mahfouf, J.F.; Noilhan, J. Comparative study of various formulations from bare soil using in situ data. *J. Appl. Meteorol.* **1991**, *30*, 1345–1365.
 18. Agustí-Panareda, A.; Balsamo, G.; Beljaars, A. Impact of improved soil moisture on the ECMWF precipitation forecast in West Africa. *Geophysical Research Letters* **2010**, *37*. doi:<https://doi.org/10.1029/2010GL044748>.
 19. Balsamo, G.; Agustí-Panareda, A.; Albergel, C.; Arduini, G.; Beljaars, A.; Bidlot, J.; Blyth, E.; Boussez, N.; Boussetta, S.; Brown, A.; Buizza, R.; Buontempo, C.; Chevallier, F.; Choulga, M.; Cloke, H.; Cronin, M.F.; Dahoui, M.; De Rosnay, P.; Dirmeyer, P.A.; Drusch, M.; Dutra, E.; Ek, M.B.; Gentine, P.; Hewitt, H.; Keeley, S.P.; Kerr, Y.; Kumar, S.; Lupu, C.; Mahfouf, J.F.; McNorton, J.; Mecklenburg, S.; Mogensen, K.; Muñoz-Sabater, J.; Orth, R.; Rabier, F.; Reichle, R.; Ruston, B.; Pappenberger, F.; Sandu, I.; Seneviratne, S.I.; Tietsche, S.; Trigo, I.F.; Uijlenhoet, R.; Wedi, N.; Woolway, R.I.; Zeng, X. Satellite and In Situ Observations for Advancing Global Earth Surface Modelling: A Review. *Remote Sensing* **2018**, *10*. doi:10.3390/rs10122038.
 20. Reichstein, M.; Camps-Valls, G.; Stevens, B.; Jung, M.; Denzler, J.; Carvalhais, N.; Prabhat. Deep learning and process understanding for data-driven Earth system science. *Nature* **2019**, *566*, 195–204.
 21. Best, M.J.; Abramowitz, G.; Johnson, H.R.; Pitman, A.J.; Balsamo, G.; Boone, A.; Cuntz, M.; Decharme, B.; Dirmeyer, P.A.; Dong, J.; Ek, M.; Guo, Z.; Haverd, V.; van den Hurk, B.J.J.; Nearing, G.S.; Pak, B.; Peters-Lidard, C.; Santanello, J.A.; Stevens, L.; Vuichard, N. The Plumbing of Land Surface Models: Benchmarking Model Performance. *Journal of Hydrometeorology* **01 Jun. 2015**, *16*, 1425 – 1442. doi:10.1175/JHM-D-14-0158.1.
 22. Houghton, N.; Abramowitz, G.; Pitman, A.J.; Or, D.; Best, M.J.; Johnson, H.R.; Balsamo, G.; Boone, A.; Cuntz, M.; Decharme, B.; Dirmeyer, P.A.; Dong, J.; Ek, M.; Guo, Z.; Haverd, V.; van den Hurk, B.J.J.; Nearing, G.S.; Pak, B.; Santanello, J.A.; Stevens, L.E.; Vuichard, N. The Plumbing of Land Surface Models: Is Poor Performance a Result of Methodology or Data Quality? *Journal of Hydrometeorology* **01 Jun. 2016**, *17*, 1705 – 1723. doi:10.1175/JHM-D-15-0171.1.
 23. Schellekens, J.; Dutra, E.; Martínez-de la Torre, A.; Balsamo, G.; van Dijk, A.; Sperna Weiland, F.; Minvielle, M.; Calvet, J.C.; Decharme, B.; Eisner, S.; Fink, G.; Flörke, M.; Peßenteiner, S.; van Beek, R.; Polcher, J.; Beck, H.; Orth, R.; Calton, B.; Burke, S.; Dorigo, W.; Weedon, G.P. A global water resources ensemble of hydrological models: the earthH2Observe Tier-1 dataset. *Earth System Science Data* **2017**, *9*, 389–413. doi:10.5194/essd-9-389-2017.
 24. Balsamo, G.; Albergel, C.; Beljaars, A.; Boussetta, S.; Brun, E.; Cloke, H.; Dee, D.; Dutra, E.; Muñoz Sabater, J.; Pappenberger, F.; de Rosnay, P.; Stockdale, T.; Vitart, F. ERA-Interim/Land: a global land surface reanalysis data set. *Hydrology and Earth System Sciences* **2015**, *19*, 389–407. doi:10.5194/hess-19-389-2015.
 25. Balsamo, G.; Engelen, R.; Thiemert, D.; Agustí-Panareda, A.; Boussez, N.; Broquet, G.; Brunner, D.; Buchwitz, M.; Chevallier, F.; Choulga, M.; van der Gon, H.D.; Florentie, L.; Haussaire, J.M.; Janssens-Maenhout, G.; M. W. Jones, T.K.; Krol, M.; Quéré, C.L.; Marshall, J.; McNorton, J.; Prunet, P.; Reuter, M.; Peters, W.; Scholze, M. The CO2 Human Emissions (CHE) project: first steps towards a

- European operational capacity to monitor anthropogenic CO₂ emissions. *Geoscientific Model Development* **2021**, *submitted*.
26. Sandu, I.; Haiden, T.; Balsamo, G.; Schmederer, P.; Arduini, G.; Day, J.; Beljaars, A.; Ben-Bouallegue, Z.; Boussetta, S.; Leutbecher, M.; Magnusson, L.; de Rosnay, P. Addressing near-surface forecast biases: outcomes of the ECMWF project 'Understanding uncertainties in surface atmosphere exchange' (USURF). *ECMWF Technical memorandum* **2020**. doi:10.21957/wxjwsojvf.
 27. Best, M.J.; Beljaars, A.C.M.; Polcher, J.; Viterbo, P. A proposed structure for coupling tiled surfaces with the planetary boundary layer. *J. Hydr. Meteorol.* **2004**, *5*, 1271–1278.
 28. Balsamo, G.; Pappenberger, F.; Dutra, E.; Viterbo, P.; van den Hurk, B. A revised land hydrology in the ECMWF model: a step towards daily water flux prediction in a fully-closed water cycle. *Hydrological Processes* **2011**, *25*, 1046–1054. doi:10.1002/hyp.7808.
 29. Boussetta, S.; Balsamo, G.; Beljaars, A.; Agusti-Panareda, A.; Calvet, J.; Jacobs, C.; van den Hurk, B.; Viterbo, P.; Lafont, S.; Dutra, E.; Jarlan, L.; Balzarolo, M.; Papale, D.; van der Werf, G. Natural land carbon dioxide exchanges in the ECMWF Integrated Forecasting System: Implementation and offline validation. *J. Geophys. Res.* **2013**, *118*, 5923–5946, DOI: 10.1002/jgrd.50488.
 30. Albergel, C.; Balsamo, G.; de Rosnay, P.; Muñoz Sabater, J.; Boussetta, S. A bare ground evaporation revision in the ECMWF land-surface scheme: evaluation of its impact using ground soil moisture and satellite microwave data. *Hydrology and Earth System Sciences* **2012**, *16*, 3607–3620.
 31. Dutra, E.; Stepanenko, V.M.; Balsamo, G.; Viterbo, P.; Miranda, P.M.A.; Mironov, D.; Schär, C. An offline study of the impact of lakes on the performance of the ECMWF surface scheme. *Boreal Env. Res.* **2010**, *15*, 100–112.
 32. Balsamo, G.; Salgado, R.; Dutra, E.; Boussetta, S.; Stockdale, T.; Potes, M. On the contribution of lakes in predicting near-surface temperature in a global weather forecasting model. *Tellus A* **2012**, *64*, 15829. doi:10.3402/tellusa.v64i0.15829.
 33. Balsamo, G. Interactive lakes in the Integrated Forecasting System. *ECMWF Newsletter, No. 137* **2013**, pp. 30–34.
 34. Loveland, T.R.; Reed, B.C.; Brown, J.F.; Ohlen, D.O.; Zhu, Z.; Youing, L.; Merchant, J.W. Development of a global land cover characteristics database and IGB6 DISCover from the 1km AVHRR data. *Int. J. Remote Sensing* **2000**, *21*, 1303–1330.
 35. Boussetta, S.; Balsamo, G.; Dutra, E.; Beljaars, A.; Albergel, C. Assimilation of surface albedo and vegetation states from satellite observations and their impact on numerical weather prediction. *Remote Sensing of Environment* **2015**, *163*, 111–126.
 36. Anderson, M.C.; Norman, J.M.; Kustas, W.P.; Li, F.; Prueger, J.H.; Mecikalski, J.R. Effects of Vegetation Clumping on Two-Source Model Estimates of Surface Energy Fluxes from an Agricultural Landscape during SMACEX. *Journal of Hydrometeorology* **01 Dec. 2005**, *6*, 892 – 909. doi:10.1175/JHM465.1.
 37. Nogueira, M.; Albergel, C.; Boussetta, S.; Johannsen, F.; Trigo, I.F.; Ermida, S.L.; Martins, J.P.A.; Dutra, E. Role of vegetation in representing land surface temperature in the CHTESSEL (CY45R1) and SURFEX-ISBA (v8.1) land surface models: a case study over Iberia. *Geoscientific Model Development* **2020**, *13*, 3975–3993. doi:10.5194/gmd-13-3975-2020.
 38. Gibelin, A.L.; Calvet, J.C.; Roujean, J.L.; Jarlan, L.; Los, S.O. Ability of the land surface model ISBA-A-gs to simulate leaf area index at the global scale: Comparison with satellites products. *Journal of Geophysical Research: Atmospheres* **2006**, *111*. doi:https://doi.org/10.1029/2005JD006691.
 39. Calvet, J.C.; Soussana, J.F. Modelling CO₂-enrichment effects using an interactive vegetation SVAT scheme. *Agricultural and Forest Meteorology* **2001**, *108*, 129 – 152. doi:https://doi.org/10.1016/S0168-1923(01)00235-0.
 40. Boone, A.; Etchevers, P. An intercomparison of three snow schemes of varying complexity coupled to the same land surface model: Local-scale evaluation at an alpine site. *J. Hydrometeorol.* **2001**, *2*, 374–394.
 41. Arduini, G.; Balsamo, G.; Dutra, E.; Day, J.J.; Sandu, I.; Boussetta, S.; Haiden, T. Impact of a Multi-Layer Snow Scheme on Near-Surface Weather Forecasts. *Journal of Advances in Modeling Earth Systems* **2019**, *11*, 4687–4710. doi:https://doi.org/10.1029/2019MS001725.
 42. Beljaars, A.; Dutra, E.; Balsamo, G.; Lemarié, F. On the numerical stability of surface-atmosphere coupling in weather and climate models. *Geoscientific Model Development Discussions* **2016**, *10*, 977–989.
 43. Calonne, N.; Flin, F.; Morin, S.; Lesaffre, B.; du Roscoat, S.R.; Geindreau, C. Numerical and experimental investigations of the effective thermal conductivity of snow. *Geophysical Research Letters* **2011**, *38*.

44. Sun, S.; Jin, J.; Xue, Y. A simple snow-atmosphere-soil transfer model. *Journal of Geophysical Research: Atmospheres* **1999**, *104*, 19587–19597.
45. Jordan, R. A one-dimensional temperature model for a snow cover: Technical documentation for SNTHERM. Technical Report CRREL Special Rep. 91-b, Cold regions research and engineering lab, Hanover, NH, 1991.
46. Brun, E.; Martin, E.; Spiridonov, V. Coupling a multi-layered snow model with a GCM. *Annals of Glaciology* **1997**, *25*, 66–72.
47. Decharme, B.; Brun, E.; Boone, A.; Delire, C.; Le Moigne, P.; Morin, S. Impacts of snow and organic soils parameterization on northern Eurasian soil temperature profiles simulated by the ISBA land surface model. *The Cryosphere* **2016**, *10*, 853–877.
48. Lawrence, D.M.; Slater, A.G.; Romanovsky, V.E.; Nicolsky, D.J. Sensitivity of a model projection of near-surface permafrost degradation to soil column depth and representation of soil organic matter. *Journal of Geophysical Research: Earth Surface* **2008**, *113*. doi:https://doi.org/10.1029/2007JF000883.
49. Stevens, D.; Miranda, P.M.A.; Orth, R.; Boussetta, S.; Balsamo, G.; Dutra, E. Sensitivity of Surface Fluxes in the ECMWF Land Surface Model to the Remotely Sensed Leaf Area Index and Root Distribution: Evaluation with Tower Flux Data. *Atmosphere* **2020**, *11*. doi:10.3390/atmos11121362.
50. Egea, G.; Verhoef, A.; Vidale, P.L. Towards an improved and more flexible representation of water stress in coupled photosynthesis-stomatal conductance models. *Agricultural and Forest Meteorology* **2011**, *151*, 1370–1384. doi:10.1016/j.agrformet.2011.05.019.
51. Verhoef, A.; Egea, G. Modeling plant transpiration under limited soil water : Comparison of different plant and soil hydraulic parameterizations and preliminary implications for their use in land surface models. *Agricultural and Forest Meteorology* **2014**, *191*, 22–32. doi:10.1016/j.agrformet.2014.02.009.
52. Orth, R.; Dutra, E.; Pappenberger, F. Improving weather predictability by including land surface model parameter uncertainty. *Monthly Weather Review* **2016**, *144*, 1551–1569. doi:10.1175/MWR-D-15-0283.1.
53. Choulga, M.; Kourzeneva, E.; Balsamo, G.; Boussetta, S.; Wedi, N. Upgraded global mapping information for earth system modelling: an application to surface water depth at the ECMWF. *Hydrology and Earth System Sciences* **2019**, *23*, 4051–4076. doi:10.5194/hess-23-4051-2019.
54. Alfieri, L.; Burek, P.; Dutra, E.; Krzeminski, B.; Muraro, D.; Thielen, J.; Pappenberger, F. GloFAS-global ensemble streamflow forecasting and flood early warning. *Hydrology and Earth System Sciences* **2013**, *17*, 1161–1175. doi:10.5194/hess-17-1161-2013.
55. Voldoire, A.; Decharme, B.; Pianezze, J.; Lebeaupin Brossier, C.; Sevault, F.; Seyfried, L.; Garnier, V.; Bielli, S.; Valcke, S.; Alias, A.; Accensi, M.; Ardhuin, F.; Bouin, M.N.; Ducrocq, V.; Faroux, S.; Giordani, H.; Léger, F.; Marsaleix, P.; Rainaud, R.; Redelsperger, J.L.; Richard, E.; Riette, S. SURFEX v8.0 interface with OASIS3-MCT to couple atmosphere with hydrology, ocean, waves and sea-ice models, from coastal to global scales. *Geoscientific Model Development* **2017**, *10*, 4207–4227. doi:10.5194/gmd-10-4207-2017.
56. Zsóter, E.; Cloke, H.; Stephens, E.; de Rosnay, P.; Muñoz-Sabater, J.; Prudhomme, C.; Pappenberger, F. How well do operational numerical weather prediction configurations represent hydrology? *Journal of Hydrometeorology* **2019**, *20*, 1533–1552. doi:10.1175/JHM-D-18-0086.1.
57. Zuo, H.; de Boisseson, E.; Zsoter, E.; Harrigan, S.; de Rosnay, P.; Wetterhall, F.; Prudhomme, C. Benefits of dynamically modelled river discharge input for ocean and coupled system. EGU General Assembly Conference Abstracts, 2020, EGU General Assembly Conference Abstracts, p. 8564.
58. Bates, P.D.; Horritt, M.S.; Fewtrell, T.J. A simple inertial formulation of the shallow water equations for efficient two-dimensional flood inundation modelling. *Journal of Hydrology* **2010**, *387*, 33–45. doi:10.1016/j.jhydrol.2010.03.027.
59. Yamazaki, D.; Kanae, S.; Kim, H.; Oki, T. A physically based description of floodplain inundation dynamics in a global river routing model. *Water Resources Research* **2011**, *47*, W04501. doi:10.1029/2010WR009726.
60. Yamazaki, D.; De Almeida, G.A.; Bates, P.D. Improving computational efficiency in global river models by implementing the local inertial flow equation and a vector-based river network map. *Water Resources Research* **2013**, *49*, 7221–7235. doi:10.1002/wrcr.20552.
61. Yamazaki, D.; O’Loughlin, F.; Trigg, M.A.; Miller, Z.F.; Pavelsky, T.M.; Bates, P.D. Development of the Global Width Database for Large Rivers. *Water Resources Research* **2014**, *50*. doi:10.1002/2013WR014664.
62. Yamazaki, D.; Lee, H.; Alsdorf, D.E.; Dutra, E.; Kim, H.; Kanae, S.; Oki, T. Analysis of the water level dynamics simulated by a global river model: A case study in the Amazon River. *Water Resources Research* **2012**, *48*, W09508. doi:10.1029/2012WR011869.

63. Decharme, B.; Delire, C.; Minvielle, M.; Colin, J.; Vergnes, J.P.; Alias, A.; Saint-Martin, D.; Séférian, R.; Sénési, S.; Voldoire, A. Recent Changes in the ISBA-CTRIP Land Surface System for Use in the CNRM-CM6 Climate Model and in Global Off-Line Hydrological Applications. *Journal of Advances in Modeling Earth Systems* **2019**, *11*, 1207–1252. doi:10.1029/2018MS001545.
64. Yamazaki, D.; Ikeshima, D.; Sosa, J.; Bates, P.D.; Allen, G.H.; Pavelsky, T.M. MERIT Hydro: A High-Resolution Global Hydrography Map Based on Latest Topography Dataset. *Water Resources Research* **2019**, *55*, 5053–5073. doi:10.1029/2019WR024873.
65. Yamazaki, D.; Ikeshima, D.; Tawatari, R.; Yamaguchi, T.; O’Loughlin, F.; Neal, J.C.; Sampson, C.C.; Kanae, S.; Bates, P.D. A high-accuracy map of global terrain elevations. *Geophysical Research Letters* **2017**, *44*. doi:10.1002/2017GL072874.
66. Yamazaki, D.; Sato, T.; Kanae, S.; Hirabayashi, Y.; Bates, P.D. Regional flood dynamics in a bifurcating mega delta simulated in a global river model. *Geophysical Research Letters* **2014**, *41*. doi:10.1002/2014GL059744.
67. Yamazaki, D.; Trigg, M.A.; Ikeshima, D. Development of a global ~90m water body map using multi-temporal Landsat images. *Remote Sensing of Environment* **2015**, *171*. doi:10.1016/j.rse.2015.10.014.
68. Mogensen, K.; Keeley, S.; Towers, P. Coupling of the NEMO and IFS models in a single executable. *ECMWF Technical memorandum* **2012**, *673*, 1–25. doi:10.21957/rfplwzuol.
69. Masson, V. A physically-based scheme for the urban energy budget in atmospheric models. *Boundary-layer meteorology* **2000**, *94*, 357–397.
70. Oleson, K.W.; Bonan, G.B.; Feddema, J.; Vertenstein, M. An urban parameterization for a global climate model. Part II: Sensitivity to input parameters and the simulated urban heat island in offline simulations. *Journal of Applied Meteorology and Climatology* **2008**, *47*, 1061–1076.
71. Porson, A.; Clark, P.A.; Harman, I.; Best, M.; Belcher, S. Implementation of a new urban energy budget scheme in the MetUM. Part I: Description and idealized simulations. *Quarterly Journal of the Royal Meteorological Society* **2010**, *136*, 1514–1529.
72. McNorton, J.; Arduini, G.; Bousseres, N.; Agustí-Panareda, A.; Balsamo, G.; Boussetta, S.; Choulga, M.; Hadade, I.; Hogan, R. An Urban Scheme for the ECMWF Integrated Forecasting System: Single-Column and Global Offline Application. *Journal of Advances in Modeling Earth Systems*, p. e2020MS002375.
73. Faroux, S.; Kaptué Tchuenté, A.; Roujean, J.L.; Masson, V.; Martin, E.; Moigne, P.L. ECOCLIMAP-II/Europe: A twofold database of ecosystems and surface parameters at 1 km resolution based on satellite information for use in land surface, meteorological and climate models. *Geoscientific Model Development* **2013**, *6*, 563–582.
74. Wedi, N.P.; Polichtchouk, I.; Dueben, P.; Anantharaj, V.G.; Bauer, P.; Boussetta, S.; Browne, P.; Deconinck, W.; Gaudin, W.; Hadade, I.; Hatfield, S.; Iffrig, O.; Lopez, P.; Maciel, P.; Mueller, A.; Saarinen, S.; Sandu, I.; Quintino, T.; Vitart, F. A Baseline for Global Weather and Climate Simulations at 1 km Resolution. *Journal of Advances in Modeling Earth Systems* **2020**, *12*, e2020MS002192. doi:https://doi.org/10.1029/2020MS002192.
75. Bauer, P.; Quintino, T.; Wedi, N.; Bonanni, A.; Chrust, M.; Deconinck, W.; Diamantakis, M.; Düben, P.; English, S.; Flemming, J.; Gillies, P.; Hadade, I.; Hawkes, J.; Hawkins, M.; Iffrig, O.; Kühnlein, C.; Lange, M.; Lean, P.; Marsden, O.; Müller, A.; Saarinen, S.; Sarmany, D.; Sleigh, M.; Smart, S.; Smolarkiewicz, P.; Thiemert, D.; Tumolo, G.; Weihrauch, C.; Zanna, C.; Maciel, P. The ECMWF Scalability Programme: Progress and Plans. *ECMWF Technical memorandum* **2020**. doi:10.21957/gdit22ulm.
76. Jung, M.; Schwalm, C.; Migliavacca, M.; Walther, S.; Camps-Valls, G.; Koirala, S.; Anthoni, P.; Besnard, S.; Bodesheim, P.; Carvalhais, N.; Chevallier, F.; Gans, F.; Goll, D.S.; Haverd, V.; Köhler, P.; Ichii, K.; Jain, A.K.; Liu, J.; Lombardozzi, D.; Nabel, J.E.M.S.; Nelson, J.A.; O’Sullivan, M.; Pallandt, M.; Papale, D.; Peters, W.; Pongratz, J.; Rödenbeck, C.; Sitch, S.; Tramontana, G.; Walker, A.; Weber, U.; Reichstein, M. Scaling carbon fluxes from eddy covariance sites to globe: synthesis and evaluation of the FLUXCOM approach. *Biogeosciences* **2020**, *17*, 1343–1365. doi:10.5194/bg-17-1343-2020.
77. Miralles, D.G.; Holmes, T.R.H.; de Jeu, R.A.M.; Gash, J.H.; Meesters, A.G.C.A.; Dolman, A.J. Global land-surface evaporation estimated from satellite-based observations. *Hydrol. Earth Syst. Sc.* **2011**, *15*, 453–469. doi:10.5194/hess-15-453-2011.
78. Martens, B.; Miralles, D.G.; Lievens, H.; Van Der Schalie, R.; De Jeu, R.A.; Fernández-Prieto, D.; Beck, H.E.; Dorigo, W.A.; Verhoest, N.E.C. GLEAM v3: Satellite-based land evaporation and root-zone soil moisture. *Geoscientific Model Development* **2017**, *10*, 1903–1925. doi:10.5194/gmd-10-1903-2017.
79. Baldocchi, D.; Falge, E.; Gu, L.; Olson, R.; Hollinger, D.; Running, S.; Anthoni, P.; Bernhofer, C.; Davis, K.; Evans, R.; Fuentes, J.; Goldstein, A.; Katul, G.; Law, B.; Lee, X.; Malhi, Y.; Meyers, T.; Munger, W.; Oechel, W.;

- U, K.T.P.; Pilegaard, K.; Schmid, H.P.; Valentini, R.; Verma, S.; Vesala, T.; Wilson, K.; Wofsy, S. FLUXNET: A New Tool to Study the Temporal and Spatial Variability of Ecosystem-Scale Carbon Dioxide, Water Vapor, and Energy Flux Densities. *Bulletin of the American Meteorological Society* **01 Nov. 2001**, *82*, 2415 – 2434. doi:10.1175/1520-0477(2001)082<2415:FANTTS>2.3.CO;2.
80. Reichstein, M.; Falge, E.; Baldocchi, D.; Papale, D.; Aubinet, M.; Berbigier, P.; Bernhofer, C.; Buchmann, N.; Gilmanov, T.; Granier, A.; Grünwald, T.; Havránková, K.; Ilvesniemi, H.; Janous, D.; Knohl, A.; Laurila, T.; Lohila, A.; Loustau, D.; Matteucci, G.; Meyers, T.; Miglietta, F.; Ourcival, J.M.; Pumpanen, J.; Rambal, S.; Rotenberg, E.; Sanz, M.; Tenhunen, J.; Seufert, G.; Vaccari, F.; Vesala, T.; Yakir, D.; Valentini, R. On the separation of net ecosystem exchange into assimilation and ecosystem respiration: review and improved algorithm. *Global Change Biology* **2005**, *11*, 1424–1439. doi:https://doi.org/10.1111/j.1365-2486.2005.001002.x.
 81. Freitas, S.C.; Trigo, I.F.; Bioucas-Dias, J.M.; Gottsche, F. Quantifying the Uncertainty of Land Surface Temperature Retrievals From SEVIRI/Meteosat. *IEEE Transactions on Geoscience and Remote Sensing* **2010**, *48*, 523–534. doi:10.1109/TGRS.2009.2027697.
 82. Johannsen, F.; Ermida, S.; Martins, J.P.A.; Trigo, I.F.; Nogueira, M.; Dutra, E. Cold Bias of ERA5 Summertime Daily Maximum Land Surface Temperature over Iberian Peninsula. *Remote Sensing* **2019**, *11*. doi:10.3390/rs11212570.
 83. Gruber, A.; Scanlon, T.; van der Schalie, R.; Wagner, W.; Dorigo, W. Evolution of the ESA CCI Soil Moisture climate data records and their underlying merging methodology. *Earth System Science Data* **2019**, *11*, 717–739. doi:10.5194/essd-11-717-2019.
 84. Dorigo, W.; Wagner, W.; Albergel, C.; Albrecht, F.; Balsamo, G.; Brocca, L.; Chung, D.; Ertl, M.; Forkel, M.; Gruber, A.; Haas, E.; Hamer, P.D.; Hirschi, M.; Ikonen, J.; de Jeu, R.; Kidd, R.; Lahoz, W.; Liu, Y.Y.; Miralles, D.; Mistelbauer, T.; Nicolai-Shaw, N.; Parinussa, R.; Pratola, C.; Reimer, C.; van der Schalie, R.; Seneviratne, S.I.; Smolander, T.; Lecomte, P. ESA CCI Soil Moisture for improved Earth system understanding: State-of-the art and future directions. *Remote Sensing of Environment* **2017**, *203*, 185–215. Earth Observation of Essential Climate Variables, doi:https://doi.org/10.1016/j.rse.2017.07.001.
 85. Gruber, A.; Dorigo, W.A.; Crow, W.; Wagner, W. Triple Collocation-Based Merging of Satellite Soil Moisture Retrievals. *IEEE Transactions on Geoscience and Remote Sensing* **2017**, *55*, 6780–6792. doi:10.1109/TGRS.2017.2734070.
 86. Ménard, C.B.; Essery, R.; Barr, A.; Bartlett, P.; Derry, J.; Dumont, M.; Fierz, C.; Kim, H.; Kontu, A.; Lejeune, Y.; others. Meteorological and evaluation datasets for snow modelling at 10 reference sites: description of in situ and bias-corrected reanalysis data. *Earth System Science Data* **2019**, *11*, 865–880.
 87. Haiden, T.; Janousek, M.; Bidlot, J.; Buizza, R.; Ferranti, L.; Prates, F.; Vitart, F. *Evaluation of ECMWF forecasts, including the 2018 upgrade*; European Centre for Medium Range Weather Forecasts, 2018.
 88. Nogueira, M.; Boussetta, S. and Balsamo, G.; Albergel, C.; Trigo, I.F.; Johannsen, S.L.; Miralles, D.; Dutra, E. Upgrading land-cover and vegetation seasonality in the ECMWF coupled system: verification with FLUXNET sites, METEOSAT satellite land surface temperatures and ERA5 atmospheric reanalysis. *Journal of Geophysical Research (JGR)* **2021**, under review.
 89. Krinner, G.; Derksen, C.; Essery, R.; Flanner, M.; Hagemann, S.; Clark, M.; Hall, A.; Rott, H.; Brutel-Vuilmet, C.; Kim, H.; others. ESM-SnowMIP: assessing snow models and quantifying snow-related climate feedbacks. *Geoscientific Model Development* **2018**, *11*, 5027–5049.
 90. de Rosnay, P.; Iseksen, L.; Dahoui, M. Snow data assimilation at ECMWF. *ECMWF Newsletter* **2015**, *143*, 26–31. doi:https://doi.org/10.21957/lkpxq6x5.
 91. Day, J.J.; Arduini, G.; Sandu, I.; Magnusson, L.; Beljaars, A.; Balsamo, G.; Rodwell, M.; Richardson, D. Measuring the impact of a new snow model using surface energy budget process relationships. *Journal of Advances in Modeling Earth Systems* **2020**, *12*, e2020MS002144.
 92. Bauer, P.; Magnusson, L.; Thépaut, J.N.; Hamill, T.M. Aspects of ECMWF model performance in polar areas. *Quarterly Journal of the Royal Meteorological Society* **2016**, *142*, 583–596.
 93. Samaniego, L.; Kumar, R.; Attinger, S. Multiscale parameter regionalization of a grid-based hydrologic model at the mesoscale. *Water Resources Research* **2010**, *46*. doi:https://doi.org/10.1029/2008WR007327.
 94. Moreno-garcia, M.C. Intensity and form of the urban heat island in Barcelona. *International Journal of Climatology* **1994**, *14*, 705–710.
 95. Basara, J.B.; Hall Jr, P.K.; Schroeder, A.J.; Illston, B.G.; Nemunaitis, K.L. Diurnal cycle of the Oklahoma City urban heat island. *Journal of Geophysical Research: Atmospheres* **2008**, *113*.

96. Hirahara, Y.; Rosnay, P.d.; Arduini, G. Evaluation of a Microwave Emissivity Module for Snow Covered Area with CMEM in the ECMWF Integrated Forecasting System. *Remote Sensing* **2020**, *12*. doi:10.3390/rs12182946.
97. Haiden, T.; Janousek, M.; Vitart, F.; Ben-Bouallegue, Z.; Ferranti, L.; Prates, C.; Richardson, D. Evaluation of ECMWF forecasts, including the 2020 upgrade. *ECMWF Technical memorandum* **2021**. doi:10.21957/6njp8byz4.
98. Baugh, C.; de Rosnay, P.; Lawrence, H.; Jurlina, T.; Drusch, M.; Zsóter, E.; Prudhomme, C. The Impact of SMOS Soil Moisture Data Assimilation within the Operational Global Flood Awareness System (GloFAS). *Remote Sensing* **2020**, *12*. doi:10.3390/rs12091490.